Assessing a turbulent mixing scheme in diurnal warm layers considering Langmuir turbulence

Xingchi Wang,[a,b] Tobias Kukulka[a]

[a] *University of Delaware, Newark, Delaware, USA*

[b] *University of Southampton, Southampton, UK*

Corresponding author: Xingchi Wang, xingchi.wang@soton.ac.uk

Xingchi Wang's current affiliation: University of Southampton, Southampton, UK

ABSTRACT:

This study investigates how Langmuir turbulence (LT) driven by Stokes drift shear affects the heated ocean surface boundary layer (OSBL) based on turbulence-resolving large eddy simulations (LES) and assesses an analytic vertical mixing parameterization based on a simplified second-moment closure (SMC) approach. Diurnal solar heating forces OSBL shoaling to generate a diurnal warm layer (DWL) in which heat and momentum are trapped. Without LT, relatively weak turbulent mixing results in a near-surface jet that is associated with enhanced turbulent kinetic energy (TKE) production of shear-driven turbulence (ST), which approximately balances TKE dissipation rates. Conversely, LT maintains strong mixing, delaying the DWL formation and preventing the TKE dissipation enhancement by generating a less sheared jet. However, sufficiently strong heating destroys TKE to ultimately reduce mixing and to create more sheared jets, which effectively shifts the LT to a ST dominated regime. A second-moment turbulence budget analysis suggests that a) the near-surface OSBL responds rapidly to the surface forcing, b) Stokes drift impacts heat and momentum budgets in profoundly different ways, and c) buoyancy terms are to leading order negligible. Building on these findings and introducing a physics-based mixing length, we develop a simplified SMC model that can be solved for near-surface expressions for key turbulent variables and mixing coefficients in terms of known variables. For ST, these expressions are consistent with Monin-Obukhov similarity theory. For LT, these expressions reveal a fundamental dependence of turbulent variables on Stokes drift shear.

1. Introduction

The ocean surface boundary layer (OSBL) periodically shoals and warms due to daytime solar radiation under light and moderate wind speeds, generating a diurnal warm layer (DWL). This DWL persists for several hours after the heating ends and gradually erodes and disappears under the influence of cooling convection during the night. In the presence of the DWL, momentum and heat are trapped in a relatively shallow layer, restricting their penetration deeper into the ocean. Consequently, this results in an accelerated near-surface velocity (diurnal jet) with speeds up to 0.1 m/s and an increment of sea surface temperature (SST) of up to 2-3 °C (Price et al. 1986; Prytherch et al. 2013; Sutherland et al. 2016). The enhanced velocity is crucial for the horizontal transport of buoyant materials in the ocean (Kukulka et al. 2016). The diurnal variability of SST is a key factor in air-sea interaction processes, influencing extreme weather and climate change (Fairall et al. 1996; Kawai and Wada 2007; Van Sebille et al. 2020). Furthermore, the restratification process associated with the DWL modulates upper ocean turbulence, which affects the vertical transport of momentum, heat, and dissolved matters in the OSBL (Webster et al. 1996; Weller and Anderson 1996; Moulin et al. 2018). Despite extensive studies on the DWL, its parameterization, particularly under the influence of Langmuir turbulence (LT) driven by surface wave-induced Stokes drift, remains limited. A key challenge lies in incorporating the LT effects into traditional mixing schemes. Large et al. (2019a, 2021) extend the Monin-Obukhov similarity theory (MOST, Monin and Obukhov 1954) to resolve LT effects. A recent study validates the capability of a second-moment closure (SMC) mixing model considering LT in reproducing LT dynamics (Schmitt et al. 2024). Motivated by this, we simplify an SMC model to retain key dynamics within the LT-driven surface layer, validated using large eddy simulation (LES) results, with the aim of improving our understanding of OSBL dynamics under LT and heating conditions.

In low wind conditions associated with a weakly turbulent OSBL, the DWL is thin, with a depth of 1-2 m and maximum stratification at the ocean surface (Soloviev and Lukas 1997; Hughes et al. 2020a). We focus on moderate wind conditions accompanied by a fully turbulent OSBL. In this scenario, turbulence distributes the injected solar radiation to greater depths (Hughes et al. 2020b), forming a deeper DWL with a depth of approximately 10 to 20 m. Unlike the low wind scenario, which exhibits minimal turbulence, the DWL in the moderate wind scenario results from the competition between heating-induced stabilization and turbulence driven by wind and wave forcing. Previous observations have shown that strong stratification reduces turbulence intensity in the OSBL (Webster et al. 1996; Weller and Anderson 1996). Conversely, strong turbulence leads to a deeper DWL and can even prevent DWL formation (Soloviev and Lukas 1997; Kawai and Wada 2007). The interaction between stratification and turbulence is crucial in determining the characteristics and evolution of the DWL under moderate wind conditions.

Recent microstructure measurements have significantly contributed to the understanding of DWL dynamics. These studies report enhanced near-surface turbulent dissipation around the heating peak (Moulin et al. 2018; Sutherland et al. 2016), which is thought to be related to the Kelvin-Helmholtz shear instability generated by the diurnal jet (Soloviev and Lukas 2013). However, the growth of this shear instability is limited under more stratified conditions, even in cases with a small Richardson number (Hughes et al. 2021). These studies reveal the transient nature of the DWL and highlight the need for further investigation to better understand the complex interaction among stratification, shear instability, and turbulence in the development and evolution of the DWL, particularly LT effects, which have not been explicitly considered in these studies.

Despite improved understanding of DWL dynamics from recent observations, wave effects are usually not included because they are challenging to assess directly in field experiments. Nevertheless, ocean surface gravity waves play a key role in the OSBL mixing, leading to nonlocal transport. These wave effects control OSBL turbulence in two primary ways: (1) wave breaking injects turbulent kinetic energy (TKE) into the near-surface ocean layer, resulting in strong mixing that diminishes significantly within one significant wave height (Terray et al. 1996); (2) non-breaking surface gravity wave-induced Stokes drift interacts with wind-generated Eulerian current shear to generate LT, efficiently mixing ocean properties throughout the OSBL (Craik and Leibovich 1976; Thorpe 2004). To focus on the LT effects, this study does not explicitly include wave breaking effects.

The dynamics of LT have been successfully investigated through the turbulence-resolving LES model based on the filtered Craik-Leibovich equation (Skyllingstad and Denbo 1995). The LES model successfully captures important observed LT features (e.g., McWilliams et al. 1997; McWilliams and Sullivan 2000; Grant and Belcher 2009), such as enhanced vertical velocities (Gargett et al. 2004; Weller et al. 1985) and organized surface convergent regions (Farmer and Li 1995; Plueddemann et al. 1996). Additionally, some hypotheses about LT obtained through LES experiments have been confirmed by observations (e.g., Gargett and Wells 2007; D'Asaro et al. 2014; Gargett and Grosch 2014; Wang et al. 2022). Regarding the interaction between LT and diurnal heating, LES studies suggest that LT-induced strong mixing usually leads to a deeper and less stratified DWL (Min and Noh 2004; Kukulka et al. 2013; Pearson et al. 2015), which has recently been demonstrated by observations in conjunction with LES (Wang et al. 2023).

It is still challenging to accurately incorporate DWL dynamics in general ocean models with LT. In those models, turbulent fluxes within the OSBL are typically parameterized through Reynolds-Averaged Navier-Stokes (RANS) models. Many of the RANS models are built upon the MOST, an important scaling near the ocean surface (i.e., upper 10% of OSBL). MOST states that the non-dimensional vertical gradients of velocity and scalar are functions of a dimensionless height within the near-surface layer, under horizontally homogeneous and stationary conditions. However, several factors could lead to deviations of MOST from observations, such as wave effects and penetrative effects of heating (Fox-Kemper et al. 2022).

Several studies have integrated LT effects into RANS models and confirmed their importance in controlling the profiles of OSBL properties (e.g., Reichl et al. 2016; Harcourt 2013; Li and Fox-Kemper 2017; Zheng et al. 2021). However, these parameterizations are predominantly tested under non-heating conditions, and their applicability under heating conditions still requires further development and assessment. Recently, Large et al. (2019a) extends the traditional MOST scaling by introducing a surface-layer bulk parameter to include the LT effects. This surface scaling is later applied to K-profile parameterization model to reproduce the evolution of DWL with LT effects (Large et al. 2021). Moreover, Schmitt et al. (2024) utilize a SMC-LT model proposed by Harcourt (2015) to examine the LT effects and propose key non-dimensional parameters for DWL evolution at different latitudes. Previous studies indicate the commonalities between MOST and the SMC model (e.g., Brost and Wyngaard 1978; Craig 1996; Kantha and Clayson 2004; Zheng 2023). The success in reproducing the DWL evolution in Large et al. (2021) and Schmitt et al. (2024) encourages the application of these commonalities to LT conditions, which is critical for improving our understanding and parameterization of LT-driven processes. Notably, several studies emphasize the critical role of the Coriolis force in determining the depth and parameterization of the DWL (Noh and Choi 2018; Wang et al. 2023; Schmitt et al. 2024). However, within the near-surface layer, where our scaling is focused, the profiles of velocity shear and stratification are less affected by the Coriolis force due to the large Rossby number associated with the small length scale.

Using the LES approach and a simplified SMC model, we examine key DWL dynamics with and without LT. Guided by solutions of our simplified model, we develop scaling of the near-surface layer under heating and LT conditions. The structure of this work is as follows: Section 2 introduces the LES model and methods used in this study, along with the experimental settings. Section 3 presents our simplified, analytically solved second-moment mixing model and discusses key findings from this model. Section 4 utilizes LES results to examine the key characteristics of the OSBL during diurnal heating for both shear-driven turbulence (ST, without wave) and LT. In Section 5, we compare near-surface-layer results calculated from LES and scaling based on the simplified SMC model. Finally, the study concludes with Section 6.

2. Methods

a. LES Model

This study conducts turbulent-resolving LES experiments based on the Craik-Leibovich equation (McWilliams et al. 1997) under heating conditions. The LES approach decomposes oceanic variables (e.g., current velocity, temperature, and pressure) into resolved components and subgrid-scale components (Moeng 1984; Sullivan et al. 1996).

We adopt the LES experiments used in Wang et al. (2023), including two transient experiments driven by time-varying diurnal heat flux and over 40 stationary experiments driven by constant forcings. For the transient experiments, the heat flux Q consists of a penetrative heat flux I_0 and a non-penetrative heat flux Q_0. The penetrative heat flux at each depth is expressed as,

$$I(z) = I_0\left(Re^{z/\zeta_1} + (1-R)e^{z/\zeta_2}\right), \tag{1}$$

where $R = 0.62$, $\zeta_1 = 1.5$ m, and $\zeta_2 = 20$ m are constant coefficients (Paulson and Simpson 1977). z indicates the vertical Cartesian coordinate positive upward with $z = 0$ at the ocean surface. The non-penetrative heat flux is only applied for cooling conditions, thus $Q = Q_0$ when $Q < 0$ and $Q = I_0$ when $Q > 0$.

Both transient experiments are driven by the same friction velocity u_* and Q, with the only difference being the inclusion of LT. The wave effect for LT is described by monochromatic waves, with the Stokes drift expressed as $u^s(z) = U^s e^{2kz}$, where U^s is surface Stokes drift and $k = 2\pi/\lambda$ is wavenumber corresponding to a constant wavelength of $\lambda = 60$ m (McWilliams et al. 1997). For transient cases, the wind and wave forcing are held constant, with $u_* = 0.0061$ m/s and $U^s = 0.068$ m/s, representing typical open ocean LT conditions with a turbulent Langmuir number of $La_t = \sqrt{u_*/U^s} = 0.3$ (Belcher et al. 2012). During the diurnal heating cycle, Q gradually increases from initial cooling with $Q = -200$ W/m^2 to peak heating with $Q = 500$ W/m^2 within 8 hours, and then decreases to the initial cooling value over the subsequent 8 hours. Notably, the heat flux imposed on our LES is expressed as the kinematic heat flux $Q/(\rho c_p)$. To clearly show the heating level, we convert it to the standard heat flux Q.

For stationary experiments, the forcings consist of various combinations of heat flux, friction velocity, and surface Stokes drift velocity for monochromatic waves with $\lambda = 60$ m (Table 1). Heat fluxes in the stationary experiments are penetrative (i.e., $Q = I_0$). Most experiments are driven by a wind forcing of $u_* = 0.0061$ m/s, so that the change in La_t primarily is controlled by the wave effects. Additionally, to focus on the heating effects, the wind and wave are aligned for both transient and stationary simulations.

The domain size of the transient and stationary LES experiments is [150, 150, 90] m. In order to capture the small-scale turbulence under strong heating conditions, most of the LES experiments use resolution with [500, 500, 720] evenly-spaced grid points for the along-wind, crosswind, and vertical directions, respectively. Some experiments conducted under weak heating conditions use a relatively coarse resolution of [250, 250, 360] grid points (Table 1). Sensitivity tests have been deployed to validate the chosen domain and resolutions, and our diagnostic analysis confirms that our resolution resolves at least 85% of TKE and is generally smaller than the Ozmidov scale in the vertical. A constant Coriolis parameter of $f = 0.0001$ 1/s is used for the LES simulations, with sensitivity tests conducted to evaluate the effects of Coriolis forcing (Table 1). These sensitivity tests for different f indicate obvious Coriolis effects on the DWL depth, while showing negligible effects on the near-surface layer, where MOST is usually applicable (Appendix A1). The initial mixed layer depth of all simulations is 50 m, over a thermocline with temperature gradient of 0.04 °C/m. All simulations spin up for 12 hours with their initial forcing to stabilize turbulence.

TABLE 1. Forcing description for stationary LES experiments, including wind speed at 10 m (U_{10}), friction velocity (u_*), turbulent Langmuir number (La_t), surface Stokes drift (U^s), and solar radiation at the ocean surface (I_0). Simulations with coarse resolution are denoted by the superscript *, while those with finer resolution are presented without this superscript. The superscript $^+$ indicates simulation driven by additional Coriolis parameters of $f = 0.00005$ 1/s and $f = 0.00014$ 1/s.

U_{10} (m/s)	u_* (m/s)	La_t	U^s (m/s)	I_0 (W/m^2)
5	0.0061	0.2	0.153	200, 500, 700
5	0.0061	0.3	0.068	0*, 25*, 50*, 100, 200, 500$^+$, 700, 1200
5	0.0061	0.4	0.038	100, 200, 300, 500, 700, 1200
5	0.0061	0.45	0.03	0*, 25*, 50*, 100, 200, 500
5	0.0061	0.52	0.023	0*, 25*, 50*, 100, 200, 500
5	0.0061	0.7	0.012	0*, 25*, 100
5	0.0061	0.9	0.008	25*, 100
5	0.0061	∞	0	0*, 50, 200, 500
7	0.0087	0.3	0.096	0*, 100, 200, 500, 700
7	0.0087	0.36	0.068	100, 200, 500

b. MOST Scaling and Modifications for Penetrative Heating

In MOST, the profiles of mean velocity shear and temperature gradient are expressed as:

$$\begin{aligned}\frac{\partial \overline{u}}{\partial z} &= \frac{u_*}{\kappa z}\phi_m,\\ \frac{\partial \overline{\theta}}{\partial z} &= \frac{\theta_*}{\kappa z}\phi_s,\end{aligned} \tag{2}$$

where overbar denotes the horizontal average; u is velocity and its direction is not considered in the MOST scaling; θ is the potential temperature and $\theta_* = Q/(c_p\rho_0 u_*)$; ϕ_m and ϕ_s are the stability functions, expressed as:

$$\phi_{m,s} = 1 + C_\phi \frac{|z|}{l_{MO}}, \tag{3}$$

for stable conditions with $|z|/l_{MO} \geq 0$. C_ϕ is empirical coefficient and varies for different conditions and studies (Wyngaard 2010). l_{MO} is the Monin-Obukhov (MO) length, defined as:

$$l_{MO} = \frac{u_*^3 c_p \rho_0}{\kappa \alpha g Q}, \tag{4}$$

where $\kappa = 0.4$ is von Kármán constant; α is the thermal expansion coefficient of seawater; c_p is the heat capacity; $\rho_0 = 1024\ \mathrm{kg/m^3}$ is the typical seawater density; and $g = 9.81\ \mathrm{m/s^2}$ is the gravitational acceleration.

The traditional MOST is designed for scenarios where heating is applied directly at the ocean surface. However, in the natural ocean, heating is penetrative due to the solar radiation, distributing heat vertically even without turbulence. Compared to penetrative heating, surface heating generates a steeper near-surface density gradient, resulting in a water column with a greater potential energy anomaly (PEA). Furthermore, penetrative heating can reach below shallower DWL, reducing heating effects in the DWL. These impacts suggest that traditional MOST overestimates heating effects when directly applied to penetrative heating conditions.

To incorporate the penetrative heating effects, we modify MOST based on PEA, similar to the method used in Schmitt et al. (2024). Here, we consider a still water column exposed to surface or penetrative heating over a time period, t_0. Assuming the column is subsequently homogenized by turbulence, we use PEA as a proxy for heating effects on the ocean stratification. Given a linear relationship between density and temperature, PEA is expressed as:

$$\begin{aligned} PEA &= \int_{-h}^{0} (\rho_m - \rho_h) g z dz \\ &= \frac{\alpha g t_0}{c_p \rho_0} \int_{-h}^{0} \left(\frac{\partial I}{\partial z} - \frac{I_0 - I(-h)}{h} \right) z dz, \end{aligned} \tag{5}$$

where ρ_h represents the density profile of the heated water column, and ρ_m is the average density of ρ_h between the surface and boundary layer depth h. For the surface heating scenario, where $\partial I/\partial z = 0$ and $I(-h) = 0$, PEA reaches its maximum, indicating the strongest stratification and heating effect. Therefore, the ratio of PEA under penetrative heating to that under surface heating, denoted as R_h, can quantify the relative impact of penetrative heating on stratification compared to surface heating. Since traditional MOST is formulated for surface heating, replacing Q with

QR_h in (4) extends the MOST framework to account for penetrative heating effects, thereby accommodating both heating scenarios.

c. Eddy Viscosity and Diffusivity

In RANS models, the turbulent fluxes for momentum and heat are typically parameterized through eddy viscosity K_m and heat diffusivity K_s:

$$-\overline{\mathbf{u}'_\perp w'} = K_m \frac{\partial \overline{\mathbf{u}}_\perp}{\partial z}, \tag{6}$$

$$\overline{\theta' w'} = -K_s \frac{\partial \overline{\theta}}{\partial z}, \tag{7}$$

where $\mathbf{u} = [u, v, w]$ is the Eulerian velocity vector, prime is the deviation from the horizontal average; and $_\perp$ indicates the horizontal components. As this study focuses solely on thermal effects, we will henceforth refer to eddy heat diffusivity simply as eddy diffusivity.

For LT, a simple adjustment to the parameterization of turbulent momentum flux is to replace Eulerian velocity shear with Lagrangian velocity shear to ensure alignment between Reynolds stress and velocity shear, commonly used in LT K-profile parameterization models (e.g., McWilliams et al. 2012; Reichl et al. 2016), shown as:

$$-\overline{\mathbf{u}'_\perp w'} = K_{mL} \frac{\partial (\overline{\mathbf{u}} + \mathbf{u}^s)_\perp}{\partial z}, \tag{8}$$

where K_{mL} is the Lagrangian eddy viscosity and $K_{mL} = K_m$ for the ST case.

3. A Simplified SMC Mixing Model

To provide a simple conceptual framework for illustrating key turbulent variables along with mixing coefficients in the DWL, we introduce a mixing closure model by simplifying an SMC approach and incorporating LT effects, hereafter referred to as the simplified model. Similar to MOST, this simplified model applies to the near-surface layer, where turbulent fluxes are approximately constant, such that $-\overline{u'w'} \approx u_*^2$, $-\overline{v'w'} \approx 0$, and $-\overline{w'\theta'} \approx Q/(c_p \rho_0)$.

We start by reviewing the governing second-moment budget equations for $\overline{u'_i u'_j}$ and $\overline{u'_j \theta'}$ with LT effects following Harcourt (2013), where $i,\ j = [1,2,3]$ denote the components in the along-wind, crosswind, and vertical directions, respectively. Using simplified expressions for some budget terms, inspired by Brost and Wyngaard (1978), we derive expressions of key turbulent variables and mixing coefficients based on the simplified model.

a. Second-moment Turbulence Equations

The second-moment budget equations for turbulent momentum and heat fluxes are (Harcourt 2013)

$$\begin{aligned}\frac{\partial\overline{u_i'u_j'}}{\partial z}+\left(\overline{u}_k+u_k^s\right)\frac{\partial\overline{u_i'u_j'}}{\partial x_k}=&-\frac{\partial\overline{u_k'u_i'u_j'}}{\partial x_k}-\left(\overline{u_i'\frac{\partial p'}{\partial x_j}}+\overline{u_j'\frac{\partial p'}{\partial x_i}}\right)-\left(\overline{u_i'u_k'}\frac{\partial\overline{u}_j}{\partial x_k}+\overline{u_j'u_k'}\frac{\partial\overline{u}_i}{\partial x_k}\right)\\&-\left(\overline{u_i'u_k'}\frac{\partial u_k^s}{\partial x_j}+\overline{u_j'u_k'}\frac{\partial u_k^s}{\partial x_i}\right)-\alpha\left(g_j\overline{u_i'\theta'}+g_i\overline{u_j'\theta'}\right)\\&-f_k\left(\epsilon_{jkl}\overline{u_i'u_l'}+\epsilon_{ikl}\overline{u_j'u_l'}\right)+\nu\nabla^2\overline{u_i'u_j'}-2\nu\overline{\frac{\partial u_i'}{\partial x_k}\frac{\partial u_j'}{\partial x_k}},\end{aligned}\tag{9}$$

$$\begin{aligned}\frac{\partial\overline{u_j'\theta'}}{\partial z}+\left(\overline{u}_k+u_k^s\right)\frac{\partial\overline{u_j'\theta'}}{\partial x_k}=&-\frac{\partial\overline{u_k'u_j'\theta'}}{\partial z}-\overline{\theta'\frac{\partial p'}{\partial x_j}}-\overline{u_j'u_k'}\frac{\partial\overline{\theta}}{\partial x_k}-\overline{u_k'\theta'}\frac{\partial\overline{u}_j}{\partial x_k}-\overline{\theta'u_k'}\frac{\partial u_k^s}{\partial x_j}-\alpha g_j\overline{\theta'\theta'}\\&-f_k\epsilon_{jkl}\overline{u_l'\theta'}+\frac{\partial}{\partial x_k}\left(\kappa_\theta\overline{u_i'\frac{\partial\theta'}{\partial x_j}}+\nu\overline{\theta'\frac{\partial u_i'}{\partial x_j}}\right)-\left(\kappa_\theta+\nu\right)\overline{\frac{\partial u_i'}{\partial x_k}\frac{\partial u_j'}{\partial x_k}},\end{aligned}\tag{10}$$

where p is the generalized pressure; $g_i=[0,0,-g]$; ν and κ_θ are molecular viscosity and diffusivity; and ϵ_{jkl} is the Levi-Civita tensor. According to (9), the TKE (=$0.5\overline{u_i'u_i'}$) equation is with the form of:

$$0.5\frac{\partial q^2}{\partial t}=-\overline{u_i'w'}\frac{\partial\overline{u}_i}{\partial z}-\overline{u_i'w'}\frac{\partial u_i^s}{\partial z}+\alpha g\overline{w'\theta'}-\frac{\partial}{\partial z}\left(\frac{\overline{u_i'u_i'w'}}{2}+\overline{w'p'}\right)-\varepsilon,\tag{11}$$

where q is the turbulent velocity scale and $0.5q^2$ is defined as TKE. ε indicates the TKE dissipation rate due to ν.

b. A Simplified SMC Approach

We adopt the closure approach from Brost and Wyngaard (1978) and use their parameterizations for turbulence dissipation and pressure terms but with a modified mixing length scale as discussed below. Additionally, we neglect terms that are not of leading-order, such as those related to buoyancy and transport. However, given the key role of buoyancy under heating conditions, its effects are implicitly incorporated into a prescribed mixing length l. These assumptions will be assessed later using LES results. The budget equations for TKE, $\overline{u'w'}$, $\overline{w'^2}$, $\overline{u'^2}$, $\overline{\theta'w'}$, and $\overline{\theta'u'}$ are, respectively,

$$0 = u_*^2\frac{\partial \overline{u}}{\partial z} + u_*^2\frac{\partial u^s}{\partial z} - c_\varepsilon\frac{q^3}{l} \tag{12a}$$

$$0 = -\overline{w'^2}\frac{\partial \overline{u}}{\partial z} - \overline{u'^2}\frac{\partial u^s}{\partial z} - A_1\overline{u'w'}\frac{q}{l} \tag{12b}$$

$$0 = 2u_*^2\frac{\partial u^s}{\partial z} - \frac{2}{3}c_\varepsilon\frac{q^3}{l} - A_1\frac{q}{l}(\overline{w'^2} - \frac{q^2}{3}) \tag{12c}$$

$$0 = 2u_*^2\frac{\partial \overline{u}}{\partial z} - \frac{2}{3}c_\varepsilon\frac{q^3}{l} - A_1\frac{q}{l}(\overline{u'^2} - \frac{q^2}{3}) \tag{12d}$$

$$0 = -\overline{w'^2}\frac{\partial \overline{\theta}}{\partial z} - \overline{u'\theta'}\frac{\partial u^s}{\partial z} - B_1\overline{w'\theta'}\frac{q}{l} \tag{12e}$$

$$0 = u_*^2\frac{\partial \overline{\theta}}{\partial z} - \overline{w'\theta'}\frac{\partial \overline{u}}{\partial z} - B_1\overline{u'\theta'}\frac{q}{l} \tag{12f}$$

where c_ε, A_1, and B_1 are positive constants that have been previously specified as $c_\varepsilon = 0.139$, $A_1 = 0.51$, and $B_1 = 1.35$ (e.g., Brost and Wyngaard 1978).

We simplify the SMC approach substantially by imposing a physically motivated l that aligns with MOST and the mixing length proposed by Brost and Wyngaard (1978). Consistent with MOST, for weak heating $l \to \kappa|z|$, whereas for strong heating $l \to \kappa G_1^{-1} l_{MO}$, where $G_1 = 4.8$ is a constant coefficient adopted from the MOST stability function (Högström 1988). Interpolation between both extreme cases via the harmonic mean yields

$$l = \kappa\frac{|z|}{1 + G_1\frac{|z|}{l_{MO}}}. \tag{13}$$

Note that with LT, κ and G_1 need to be modified to take LT mixing into account. For example, one may replace l_{MO} with the Langmuir stability length for strong LT (Belcher et al. 2012), which will be assessed later based on LES results.

For given mixing length l, these six equations in (12) can be solved for the six dependent variables q, $\partial\overline{u}/\partial z$, $\overline{w'^2}$, $\overline{u'^2}$, $\partial\overline{\theta}/\partial z$, and $\overline{u'\theta'}$. According to (12a-12d), the turbulent velocity scale q can be obtained through the governing sixth order polynomial equation, expressed as:

$$\frac{q^6}{u_*^6} + \frac{12}{A_1 - 2c_\varepsilon}\frac{l}{u_*}\frac{\partial u^s}{\partial z}\frac{q^3}{u_*^3} - \frac{3A_1^2}{(A_1 - 2c_\varepsilon)c_\varepsilon}\frac{q^2}{u_*^2} - \frac{12}{(A_1 - 2c_\varepsilon)c_\varepsilon}\left(\frac{l}{u_*}\frac{\partial u^s}{\partial z}\right)^2 = 0. \tag{14}$$

This equation implies that the normalized turbulent velocity scale q/u_* can be expressed as a function of non-dimensional parameter:

$$\chi = \frac{l}{u_*}\frac{\partial u^s}{\partial z}. \tag{15}$$

Although the analytical solution of (14) is obtainable, its complexity motivates the use of a numerical solution. Thus, we define $q/u_* = F_q(\chi)$, where each χ corresponds to a unique value of $F_q(\chi)$ greater than zero (Figure 1a).

For fixed l and u_*, larger values of χ correspond to greater Stokes drift shear, which usually indicates stronger LT conditions. In the ST case (i.e., $\chi = 0$), q/u_* remains constant, consistent with classical scaling (e.g., MOST), which uses u_* as the turbulent velocity scale. In the LT case (i.e., $\chi > 0$), F_q exhibits a non-monotonic response to increasing χ. q/u_* initially decreases, reaching a minimum at approximately $\chi = 0.34$, and subsequently increases. This behavior suggests that increased LT effects do not always lead to enhanced TKE. Furthermore, the expression for χ indicates a weakening of LT effects due to strong heating. Specifically, for conditions of strong heating with fixed u_* and $\frac{\partial u^s}{\partial z}$, χ approaches zero as $l \longrightarrow 0$, leading q/u_* to converge to its ST value.

To further investigate the response of q/u_* to varying LT effects and to facilitate later comparison with LES results, we employ another insightful non-dimensional parameter:

$$\eta = u_*^2\frac{\partial u^s}{\partial z}\frac{l}{c_\varepsilon q^3} = \chi\frac{u_*^3}{c_\varepsilon q^3} = \chi\frac{F_q(\chi)^3}{c_\varepsilon} = \frac{\frac{\partial u^s}{\partial z}}{\frac{\partial u^s}{\partial z} + \frac{\partial \overline{u}}{\partial z}}. \tag{16}$$

This parameter, derived from (12a), represents the ratio of production from Stokes drift shear to that from Lagrangian shear. η is directly linked to LT strength. Stronger LT typically corresponds to larger Stokes drift shear and smaller Eulerian shear, leading to higher η. Large et al. (2019a) introduced a similar parameter for the near-surface layer (top 10% of the mixing layer). The primary difference is that η neglects buoyancy production but accounts for the depth dependence of Stokes drift. According to (16), η can be expressed as a function of χ. As shown in Figure 1a, η increases with χ but approaches a constant value for larger χ, suggesting that increased Stokes drift shear does not indefinitely enhance LT strength.

The expression for q, in terms of η, is much simpler than the solution expressed in χ,

$$\frac{q}{u_*} = \left(\frac{\frac{3A_1^2}{(A_1 - 2c_\varepsilon)c_\varepsilon}}{-\frac{12c_\varepsilon}{A_1 - 2c_\varepsilon}\eta^2 + \frac{12c_\varepsilon}{A_1 - 2c_\varepsilon}\eta + 1} \right)^{\frac{1}{4}} = \tilde{F}_q(\eta). \tag{17}$$

F with tilde indicates a function of η while F without tilde depends on χ. Similar to F_q, $\tilde{F}_q(\eta)$ first decreases and then increases. Notably, its value at $\eta = 1$ (the maximum value for the idealized model as velocity shear needs to be positive) approximately equals that of the ST case, suggesting relatively small dependence of TKE on LT strength. To further investigate this relationship, we derive the expressions for normalized velocity variance $\overline{w'^2}/u_*^2$ and $\overline{u'^2}/u_*^2$ according to (12c) and (12d), which are also functions of η:

$$\frac{\overline{w'^2}}{u_*^2} = \frac{q^2}{u_*^2}\left(\frac{A_1 - 2c_\varepsilon}{3A_1} + \frac{2c_\varepsilon}{A_1}\eta\right) = \tilde{F}_{ww}(\eta), \tag{18}$$

$$\frac{\overline{u'^2}}{u_*^2} = \frac{q^2}{u_*^2}\left(\frac{A_1 + 4c_\varepsilon}{3A_1} - \frac{2c_\varepsilon}{A_1}\eta\right) = \tilde{F}_{uu}(\eta). \tag{19}$$

These functions illuminate the LT impacts on turbulence anisotropy (McWilliams et al. 1997). Specifically, for the ST case (i.e., $\eta = 0$), $\overline{u'^2} > \overline{w'^2}$. As η increases, $\overline{w'^2}$ rises while $\overline{u'^2}$ decreases, resulting in $\overline{w'^2} > \overline{u'^2}$ for sufficiently strong LT. Throughout this process, the changes in $\overline{w'^2}$ and $\overline{u'^2}$ are non-linear. For $0 < \eta < 0.5$, $\overline{w'^2}$ increases more slowly than $\overline{u'^2}$ decreases, while for $0.5 < \eta < 1$, it increases more rapidly (Figure 1b), which results in the non-monotonic response of q.

c. Eddy Mixing Coefficients

According to the $\overline{u'w'}$ budget (12b), the eddy viscosity defined in (8) can be split into contributions from Eulerian shear K_m and Stokes drift shear K_m^s (Harcourt 2013), expressed as:

$$K_m = \frac{1}{A_1}\frac{l}{q}\overline{w'^2} = ql\left(\frac{2c_\varepsilon}{A_1^2}\eta + \frac{A_1 - 2c_\varepsilon}{3A_1^2}\right) = u_* l \tilde{F}_m(\eta), \tag{20}$$

$$K_m^s = \frac{1}{A_1}\frac{l}{q}\overline{u'^2} = ql\left(-\frac{2c_\varepsilon}{A_1^2}\eta + \frac{A_1 + 4c_\varepsilon}{3A_1^2}\right) = u_* l \tilde{F}_m^s(\eta). \tag{21}$$

By substituting the expressions of $\overline{w'w'}$ and $\overline{u'u'}$ from (18) and (19) into (12b), K_{mL} can be expressed as

$$K_{mL} = \frac{u_*^2}{\frac{\partial \overline{u}}{\partial z} + \frac{\partial u^s}{\partial z}} = ql\left(-\frac{4c_\varepsilon}{A_1^2}\eta^2 + \frac{4c_\varepsilon}{A_1^2}\eta + \frac{A_1 - 2c_\varepsilon}{3A_1^2}\right) = u_* l \tilde{F}_{mL}(\eta). \tag{22}$$

Moreover, using the $\overline{w'\theta'}$ and $\overline{u'\theta'}$ budgets, (12e) and (12f), we solve for the eddy diffusivity

$$K_s = ql\left(\frac{\eta c_\varepsilon \frac{q^2}{u_*^2} + B_1 \tilde{F}_{ww}(\eta)}{\eta(\eta - 1)c_\varepsilon^2 \frac{q^6}{u_*^6} + B_1^2 \frac{q^2}{u_*^2}}\right) = u_* l \tilde{F}_s(\eta). \tag{23}$$

Consistent with (17)-(19), these mixing coefficients can be expressed as a function of η once normalized by u_* and l (Figure 1b).

For the ST case, $K_m = K_{mL}$, and K_m^s is irrelevant due to the zero Stokes drift shear. We find for the stability functions ϕ_m and ϕ_s based on the model-derived K_m and K_s

$$\phi_{m,s} = \frac{\kappa z u_*}{K_{m,s}} = \frac{1}{\tilde{F}_{m,s}(0)}\frac{\kappa z}{l} \propto 1 + G_1 \frac{|z|}{l_{MO}} \tag{24}$$

consistent with the MOST expression (3). This consistency aligns with a previous study (Zheng 2023), which shows that the MOST stability functions can be numerically solved in a classical SMC framework (Kantha and Clayson 1994), expressed in terms of z/l_{MO}. The agreement with Zheng (2023) suggests that our simplified model successfully captures the fundamental physical

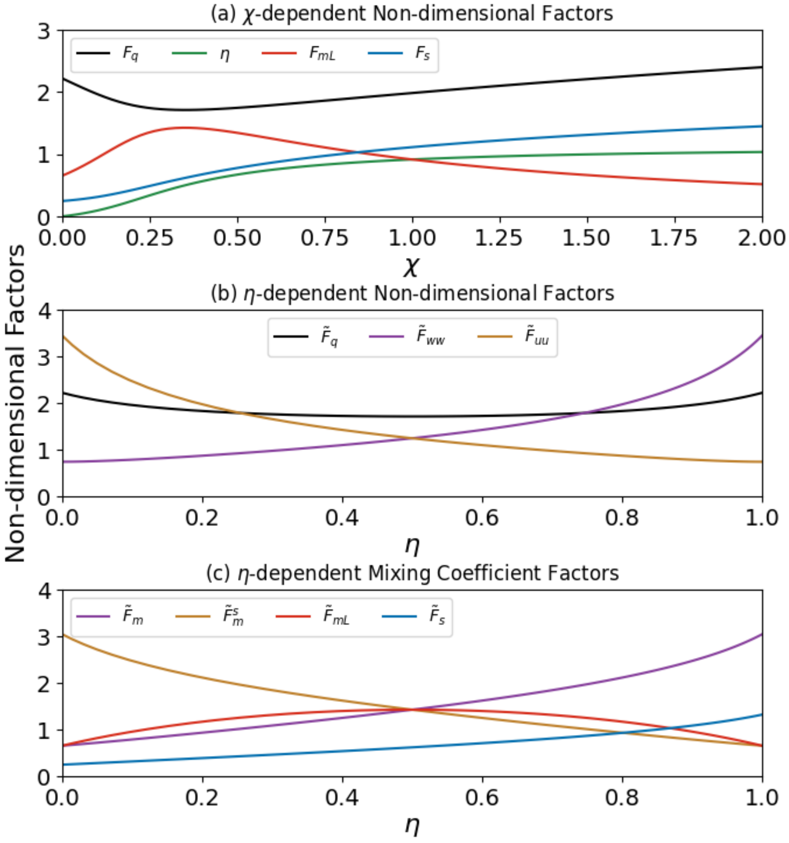

FIG. 1. The response of non-dimensional factors to non-dimensional parameters (a) χ from (15) and (b, c) η from (16). These factors are derived based on our simplified model. The results in (a) stem from the numerical solution of (14) and the results in (b, c) are solved using (17)-(23). When χ, $\eta = 0$, the results are shown for ST condition.

processes underlying the SMC framework. Since K_m is a special case of K_{mL}, we refer to K_{mL} as the eddy viscosity hereafter.

For the LT case, the mixing coefficients retain the form of MOST but exhibit varied responses to η (Figure 1c). For example, $\tilde{F}_m$ and $\tilde{F}_s$ increase with η, consistent with the fact that larger Stokes drift shear results in enhanced mixing. Conversely, $\tilde{F}_m^s$ decreases with η due to reduced $\overline{u'^2}$. The decreased $\tilde{F}_m^s$ indicates that as Stokes drift increases, the efficiency of its contribution to the turbulent stress decreases. This opposing behavior of $\tilde{F}_m$ and $\tilde{F}_m^s$ leads to an increase in $\tilde{F}_{mL}$ for small η and a decrease at large η, overall resulting in relatively small changes of $\tilde{F}_{mL}$.

Notably, the constants adopted from Brost and Wyngaard (1978) may generate inconsistencies in the mixing coefficients. A direct example of this is the Prandtl number, $Pr = K_{mL}/K_s$, which is approximately 2.6 for the ST case based on the simplified model (Figure 1c). While in MOST, Pr is typically expected to be around 1 (Businger et al. 1971; Högström 1988; Foken 2006). Using (22) and (23), we obtain that $Pr = B_2/B_1$ for $\eta = 0$, suggesting that the large value of Pr is likely due to the chosen constants. This conclusion is further supported by other SMC models. For instance, the model by Kantha and Clayson (1994) uses similar values for B_2 and B_1 to parameterize the pressure term in the SMC equations. Our study finds that the inconsistencies in mixing coefficients can be effectively addressed by adjusting the value of B_2, a correction that will be discussed in more detail in later sections.

According to (16), each η-dependent factor, $\tilde{F}_X(\eta)$, can be expressed in terms of χ, denoted as $F_X(\chi)$. This transformation arises naturally from the direct relationship between η and χ. These χ-dependent factors indicate that mixing coefficients can be expressed as functions of known u^s, u_*, and l (Figure 1a). Overall, our simplified model elucidates the fundamental characteristics of key turbulent variables and mixing coefficients for both ST and LT cases. Notably, heating effects in the momentum equations are incorporated solely through the mixing length, indicating that the findings of our simplified model are also applicable to neutral cases. In the following sections, we will use LES results to validate the assumptions of our simplified model and corroborate its findings.

4. OSBL Response to Diurnal Heating for ST and LT

In this section, we examine LES results driven by diurnal heating.

a. Evolution of Velocity, Temperature, and Turbulence

We first investigate the responses of temperature and velocity to the diurnal heating (Figure 2). During this process, the DWL depth is defined as the mixing layer depth h_b, where the magnitude of turbulent momentum flux $|\overline{\mathbf{u}'_\perp w'}|$ decreases to 5% of its surface value (i.e., $0.05u_*^2$).

For the ST case, the OSBL rapidly shoals after the heating onset ($t = 0$ h) and remains shallow and relatively stable throughout the rest of the heating period and into the cooling period (Figure 2a). This process is consistent with the morning detrainment and afternoon entrainment processes

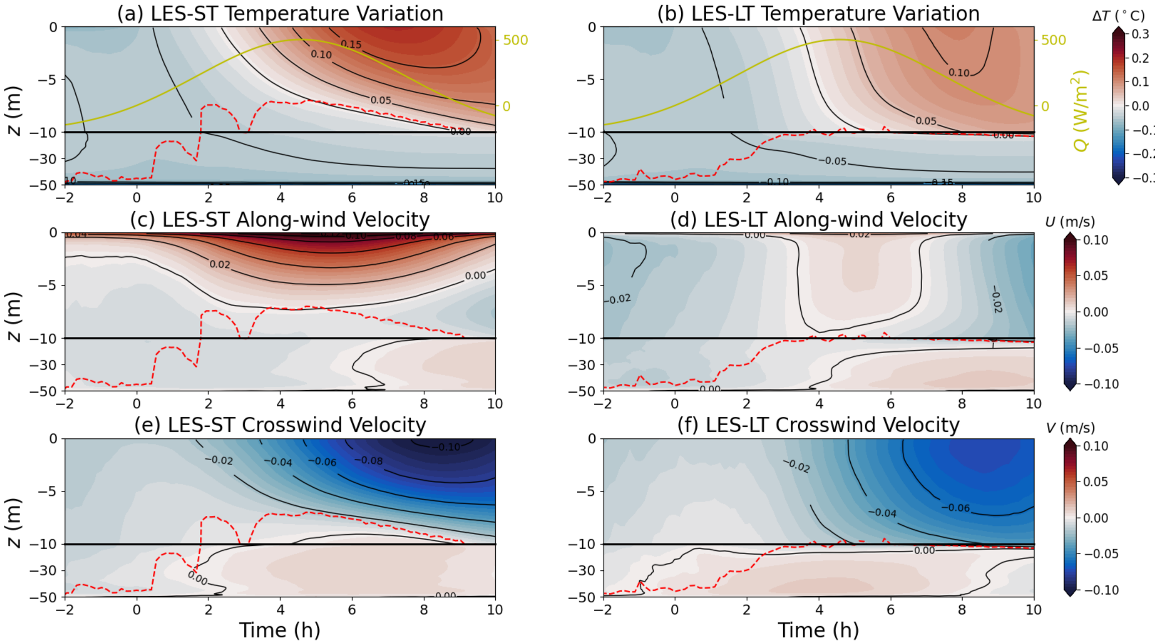

Fig. 2. OSBL evolution for (a, b) temperature, (c, d) along-wind velocity, and (e, f) crosswind velocity for the (left) ST and (right) LT cases. Red dashed lines represent the LES mixing layer depth h_b. The Y-axis is divided into two regions with distinct scalings, separated by a horizontal black line. The temperature in (a, b) is shown as the deviation from its initial value. Yellow lines in (a, b) indicate the surface heat flux Q.

reported in Large et al. (2021). We define the time of DWL formation as the end of the rapid OSBL shoaling, which occurs at approximately $t = 2$ h for the ST case. The formation of the DWL leads to significant increases in both temperature and velocity as heat and momentum fluxes are trapped within this shallow DWL (Figures 2a,c,e). Moreover, these increased temperature and velocity correspond to enhanced stratification and velocity shear compared to the period prior to the DWL formation, consistent with earlier observations and model results (e.g., Large et al. 1994; Noh et al. 2009; Sutherland et al. 2016; Moulin et al. 2018; Hughes et al. 2021).

For the LT case, the DWL forms $\sim$ 1 hour later than the ST case (Figure 2b). This delay suggests that LT suppresses the DWL formation, aligning with a previous study focusing on strong swell conditions (Kukulka et al. 2013). Compared to the ST case, both temperature and velocity in the LT case are substantially lower, with smaller vertical gradients (Figure 2). During the DWL period $(2-9$ h$)$, the time-mean and maximum SST increments for LT are reduced by 63% and 45%, respectively, compared to ST, highlighting the significant impact of LT on the diurnal warming of the ocean surface. Additionally, the mean DWL depth for ST is approximately 25% shallower than that for LT. These findings suggest that LT moderates ocean surface warming by distributing the injected heat flux more uniformly and to greater depths.

It is worth noting that the differences between the LT and ST cases, evident in the temperature and velocity profiles, are to some extent consistent with the assumptions of previous bulk mixed layer models. For example, the Price-Weller-Pinkel model, proposed by Price et al. (1986), assumes homogeneous properties within the boundary layer, akin to the LT case whose enhanced mixing leads to weak stratification and velocity shear. In contrast, the modified Price-Weller-Pinkel model (i.e., Fairall et al. 1996) assumes linear decreases in temperature and velocity with depth, which is typical of the ST case. Given the good agreement between these layer models and observational results, as confirmed in previous studies (e.g., Price et al. 1986; Fairall et al. 1996; de Boyer Montégut et al. 2004; Plueddemann and Farrar 2006), this consistency suggests that LT effects might be implicitly included in the bulk mixed layer models by defining the profiles of properties within the mixed layer.

To further elucidate the OSBL response to diurnal heating, we examine the evolution of TKE and vertical velocity variance $\overline{w'^2}$. As shown in Figure 3, TKE and $\overline{w'^2}$ decrease after the onset of heating due to increased stratification in both ST and LT cases. During the rapid OSBL shoaling, TKE and $\overline{w'^2}$ remain relatively high at greater depths due to earlier cooling. This residual turbulence reflects active mixing, which counteracts heating-induced restratification and delays the formation of the DWL. Furthermore, the higher TKE and $\overline{w'^2}$ in the LT case in the cooling period likely causes a longer delay in DWL formation compared to the ST case.

During the DWL period, $\overline{w'^2}$ in the LT case is approximately 3 to 4 times larger than in the ST case. This elevated $\overline{w'^2}$ for LT facilitates efficient vertical transport, resulting in weaker stratification. Notably, near the ocean surface ($|z| < 3$ m), TKE in the LT case shows no significant enhancement compared to the ST case and is even lower than its ST value, consistent with findings from the simplified model (Figures 1a,b).

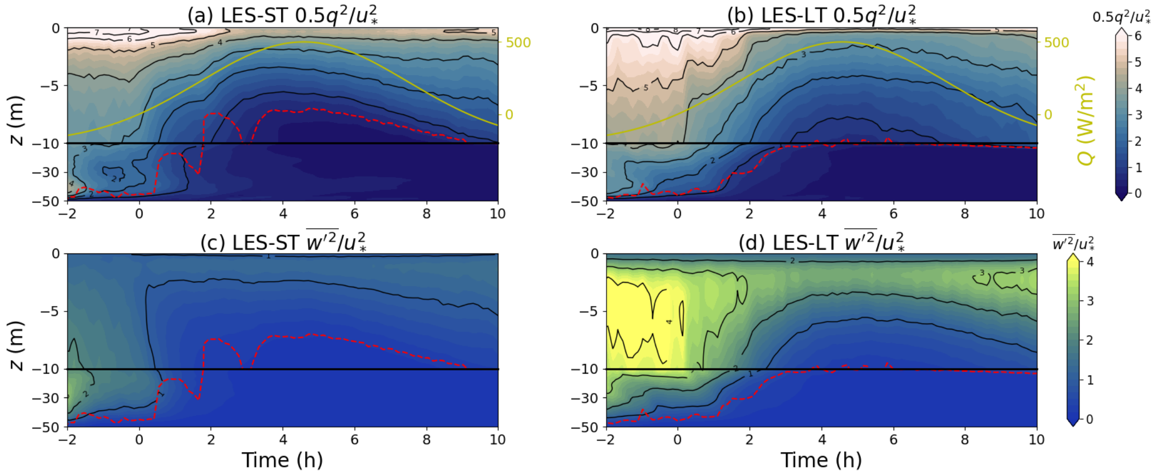

Fig. 3. The LES evolution of normalized (a,b) TKE $0.5q^2/u_*^2$ and (c,d) vertical velocity variance $\overline{w'^2}/u_*^2$ for (left) ST and (right) LT cases. The Y-axis is divided into two regions. The red and yellow lines are the same as those in Figure 2.

b. Responses of K_s and K_{mL} to Diurnal Heating

To better understand the limitations of current OSBL parameterizations during diurnal heating, we investigate the evolution of eddy viscosity (8) and diffusivity (7) for ST and LT (Figure 4). For most of the heating period, these mixing coefficients inversely correlate with Q. Additionally, they increase with depth near the surface, consistent with MOST scaling.

During the rapid shoaling of the OSBL, these coefficients remain significant due to the development of turbulence, particularly at greater depths. Shortly after the onset of heating, K_s briefly becomes negative due to the lag between the turbulence response and changes in temperature gradients. Specifically, penetrative solar radiation induces positive temperature gradients, while the turbulent heat flux, $-\overline{\theta' w'}$, remains negative due to its relatively slow response. These findings highlight the challenges in predicting this evolution based on parameterization, as previously reported by Large et al. (2019b). However, this period is typically brief and occurs only during the early heating phase, accompanied by negligible changes in temperature and velocity, as shown in Figure 2.

Figure 4 reveals clear differences in mixing coefficients between the ST and LT cases. In the LT case, K_{mL} and K_s exceed their ST counterparts, reflecting enhanced mixing driven by LT. These

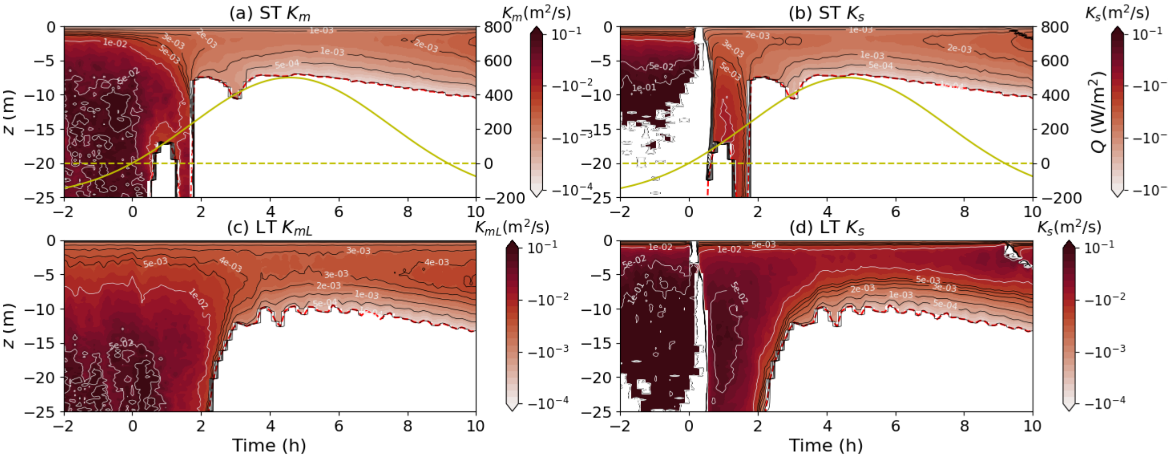

FIG. 4. (a) Eulerian eddy viscosity K_m and (b) eddy diffusivity K_s for ST and (c) Lagrangian eddy viscosity K_{mL} and (d) eddy diffusivity K_s for LT calculated by LES results. Color scales are shown in logarithmic form. Only values at depths above h_b and positive values are shown. Red and yellow lines are the same as those in Figure 2.

larger values of K_{mL} and K_s are consistent with the results of the simplified model that $\tilde{F}_{mL}$ and $\tilde{F}_s$ are smallest for the ST case (Figure 1).

To further investigate the differences between ST and LT, we calculate the turbulent Prandtl number ($Pr = K_{mL}/K_s$). For ST, Pr remains approximately constant throughout most of the DWL and is close to 1 (Figure 5a), consistent with MOST scaling. In contrast, for LT, Pr depends on both depth and heat flux. At a fixed heat flux, Pr initially decreases with depth, reaching a minimum around $z = -3$ m. At a fixed depth, Pr correlates with the heat flux. While previous parameterizations for LT often consider $Pr = 1$ when utilizing Lagrangian velocity eddy viscosity, these results highlight the need for additional focus on the variability of Pr induced by LT effects. Notably, since K_{mL} is used to calculate Pr, the small Pr observed in LT is primarily due to the Stokes drift shear, which is independent of the flow field (Large et al. 2019a). This small value does not imply that momentum mixes less than heat.

Our simplified model qualitatively explains the Pr differences between the ST and LT cases. According to (22) and (23), the simplified model predicts that Pr is constant for ST and increases with η for LT. Figure 5c shows that η, which is based on LES results, increases away from the surface, further supporting the predictions of the simplified model. Using this LES-derived η, we

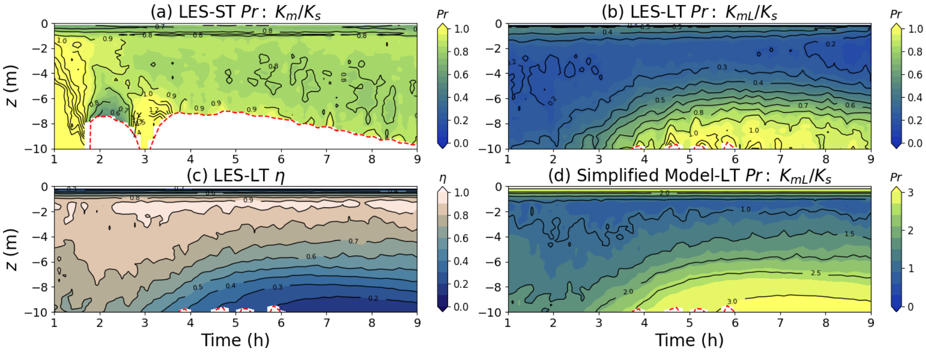

FIG. 5. The turbulent Prandtl number $Pr = K_{mL}/K_s$ derived from LES results for the (a) ST and (b) LT cases during the heating period. (c) The non-dimensional factor η for the LT case, as derived from LES results. (d) Pr calculated from the simplified model using (22) and (23), with η values derived from LES results in (c).

calculate Pr for LT based on the simplified model solution (Figure 5d), which qualitatively aligns with the LES results. For both ST and LT cases, Pr from the simplified model is larger than the LES results due to the untuned constants in the simplified model.

c. Budget Analyses for Turbulent Variables

In the simplified model (Section 3), we only consider the balance of leading-order terms in the budgets of TKE and second-moment turbulent variables. To assess the validity of these simplifications and to further elucidate the mechanism of turbulence evolution, particularly the differences with and without the wave effect, we conduct budget analyses for TKE and turbulent fluxes. For clarity, all analyzed budget terms are listed in Table 2.

Figure 6 shows the evolution of key terms in the TKE budget equation (11). We present each term with its corresponding symbol for clarity, shown as:

$$0.5\frac{\partial q^2}{\partial t} = P_E^{TKE} + P_S^{TKE} + B^{TKE} + T^{TKE} - \varepsilon + SGS, \tag{25}$$

where $0.5\partial q^2/\partial t$ is the TKE temporal changing rate; P_E^{TKE} and P_S^{TKE} represent TKE production from Eulerian velocity shear and Stokes drift shear, respectively; B^{TKE} is the buoyancy flux, which acts as a sink for TKE under heating conditions; T^{TKE} denotes TKE transport; ε is the TKE dissipation; and SGS represents the sum of minor subgrid-scale terms (Table 2).

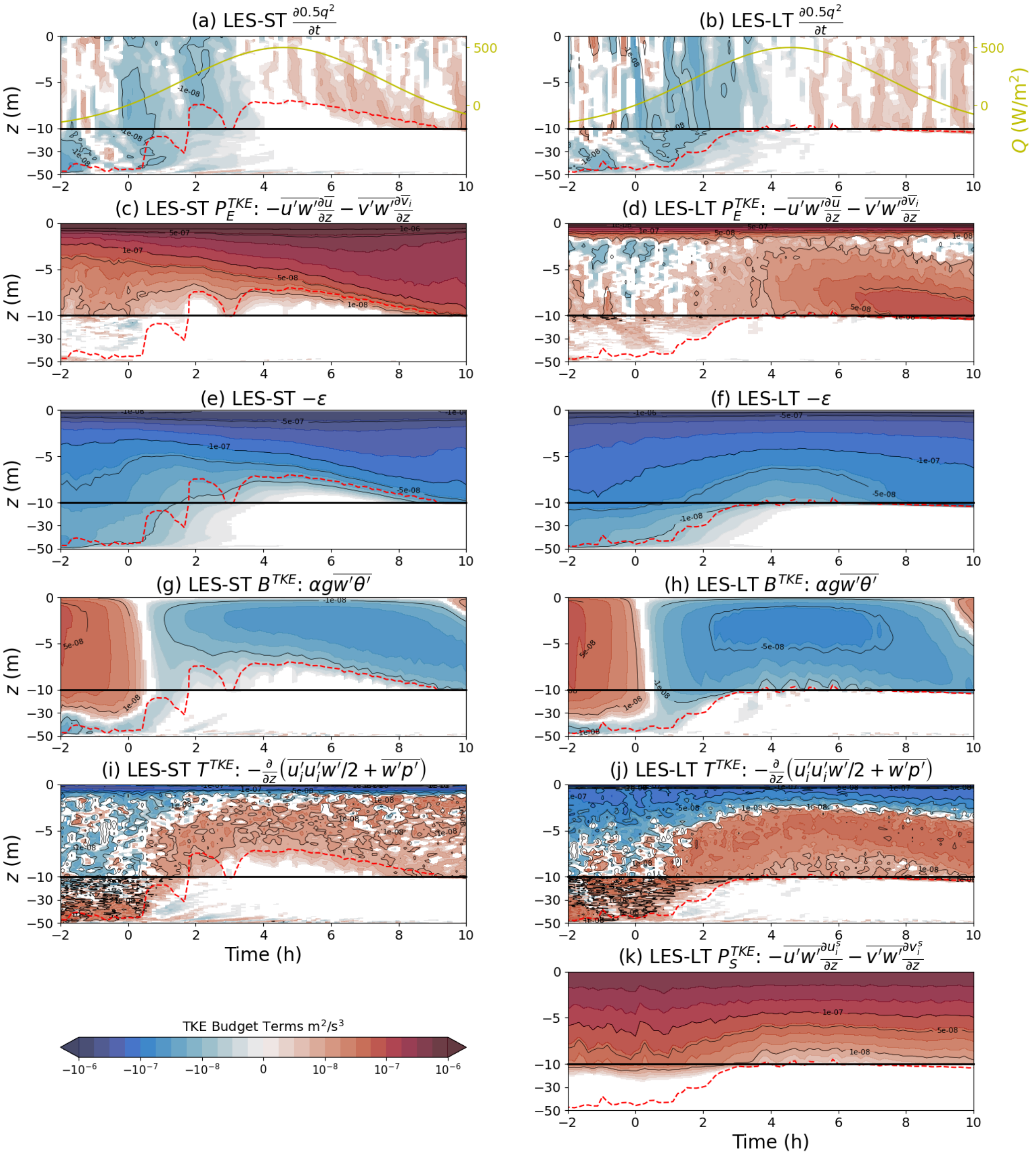

FIG. 6. The evolution of TKE budget terms based on LES results, as described in (11): (a, b) TKE changing rate, (c, d) Eulerian shear production P_E, (e, f) TKE dissipation rate ε, (g, h) buoyancy term B, (i, j) gradients of TKE transport T, and (k) Stokes production P_S for (left) ST and (right) LT. The Y-axis is divided into two regions, and the red and yellow lines are the same as those in Figure 2. Colors are displayed in logarithmic form and values smaller than 10^{-9} are considered as 0.

TABLE 2. A list of budget terms analyzed in Section 4c, including their symbols, mathematical expressions, descriptions, and corresponding locations.

Symbol	Mathematic Expression	Describtion	Location of Associated Equation and Figure
P_E^{TKE}	$-\overline{u'w'}\frac{\partial \overline{u}}{\partial z} - \overline{v'w'}\frac{\partial \overline{v}}{\partial z}$	TKE production from Eulerian velocity shear	(25), Figure 6
P_S^{TKE}	$-\overline{u'w'}\frac{\partial u^s}{\partial z} - \overline{v'w'}\frac{\partial v^s}{\partial z}$	TKE production from Stokes drift velocity shear	(25), Figure 6
B^{TKE}	$\alpha g\overline{w'\theta'}$	Buoyancy flux	(25), Figure 6
T^{TKE}	$\frac{\partial}{\partial z}\left(\frac{\overline{u_i'u_i'w'}}{2}+\overline{w'p'}\right)$	Vertical gradient of TKE transport	(25), Figure 6
ε		TKE dissipation rate due to molecular viscosity	(25), Figure 6
P_E^{uw}	$\overline{w'w'}\frac{\partial \overline{u}}{\partial z}$	Turbulent stress production from Eulerian velocity shear	(26), Figure 7
P_S^{uw}	$\overline{u'u'}\frac{\partial u^s}{\partial z}$	Turbulent stress production from Stokes drift velocity shear	(26), Figure 7
B^{uw}	$-\alpha g\overline{u'\theta'}$	Turbulent stress contribution due to buoyancy	(26), Figure 7
Π^{uw}	$\overline{u'\frac{\partial p'}{\partial z}}+\overline{w'\frac{\partial p'}{\partial x}}$	Turbulent stress contribution due to pressure	(26), Figure 7
$P_\theta^{\theta w}$	$-\overline{w'w'}\frac{\partial \overline{\theta}}{\partial z}$	Turbulent heat flux production from temperature gradient	(27), Figure 8
$P_S^{\theta w}$	$-\overline{u'\theta'}\frac{\partial u^s}{\partial z}$	Turbulent heat flux production from Stokes drift velocity shear	(27), Figure 8
$B^{\theta w}$	$\alpha g\overline{\theta'\theta'}$	Turbulent heat flux contribution due to buoyancy	(27), Figure 8
$\Pi^{\theta w}$	$-\overline{\theta'\frac{\partial p'}{\partial z}}$	Heat flux contribution due to pressure	(27), Figure 8

For both ST and LT cases, $0.5\partial q^2/\partial t$ is negligible compared to other major terms, except at greater depth during the rapid OSBL shoaling (Figures 6a,b). This suggests that turbulence in the upper OSBL remains quasi-stationary during diurnal heating, with transient effects only significant at greater depths. This quasi-stationary process supports the validity of our simplified model, which focuses on the surface layer.

In the ST case, the primary balance is between P_E^{TKE} and $-\varepsilon$ (Figures 6c,e). During the heating period, the magnitudes of B^{TKE} and T^{TKE} are approximately one order of magnitude smaller than those dominant terms (Figures 6g,i), particularly in the upper DWL. B^{TKE} exhibits a convex vertical profile due to the penetrative heating (Pearson et al. 2015), with a maximum around $z = -3$ m. However, during the detrainment period, B^{TKE} becomes a critical sink term for TKE, substantially contributing to the decay of turbulence.

For the LT case, the primary balance is between P_S^{TKE} and $-\varepsilon$, with P_E^{TKE} being significant near the surface (Figures 6d,f,k). Furthermore, P_E^{TKE} exceeds P_S^{TKE} at the base of the DWL for $t > 6$ h, indicating the dominant role of shear instabilities in the entrainment process, consistent with previous work (Kukulka et al. 2010). Compared to the ST case, B^{TKE} and T^{TKE} are larger in the LT case, suggesting stronger vertical transport due to LT, although still much smaller than the dominant terms in the upper OSBL.

In the ST case, ε undergoes an enhancement during diurnal heating, which is attributed to the increased P_E^{TKE} due to increased velocity shear associated with the diurnal jet (Figures 2c,e), consistent with microstructure observations from Sutherland et al. (2016). However, this enhancement in ε is not observed in the LT case (Figure 6f), which arises from the nearly constant P_S^{TKE} because of the imposed Stokes drift velocity and the approximately constant turbulent stress (Figure 6k). Notably, as heating increases, the changes in P_S^{TKE} and P_E^{TKE} indicate a decreasing importance of LT, consistent with the response of η to χ in the simplified model. Using LES under varying heating and LT conditions (Appendix A2), we find that the LT effect varies with heat flux. Specifically, for a constant La_t, the dominance of Stokes production typically decreases as the normalized MO length scale $l_{MO} f / u_*$ decreases (i.e., under strong heating conditions), indicating a weakening of the LT effect.

Next, we examine the turbulent stress budgets. Since the turbulent stress generally aligns with the Lagrangian velocity shear, which is approximately in the along-wind direction, we focus on the budget for $-\overline{u'w'}$, with its simplified form given by:

$$\frac{\partial - \overline{u'w'}}{\partial t} = P_E^{uw} + P_S^{uw} + B^{uw} + \Pi^{uw} + SGS. \qquad (26)$$

where the left-hand side represents the temporal changing rate of turbulent stress; the first four terms on the right-hand side correspond to the contributions from Eulerian velocity shear, Stokes drift shear, buoyancy, and pressure (as detailed in Table 2); the last term, SGS, represents the sum of subgrid-scale terms and other minor contributions such as those due to Coriolis force.

Similarly to TKE, the primary production terms for $-\overline{u'w'}$ are P_E^{uw} in the ST case and P_S^{uw} in the LT case, both of which are approximately balanced by the pressure term Π^{uw}. Although P_E^{uw} in the LT case is small near mid-depth of the DWL, it contributes significantly near the surface and at the DWL base (Figure 7b). Notably, P_E^{uw} below 2 m depth is negative, opposed to P_S^{uw}, indicating a suppression effect on the turbulent stress development. This negative P_E^{uw} may result from the non-local transport where $\partial u / \partial z < 0$, which induces Eulerian shear opposite the wave direction

(McWilliams et al. 2014). Additionally, P_E^{uw} becomes positive near the heating peak, as strong heating weakens the LT mixing causing the Eulerian velocity to become more sheared.

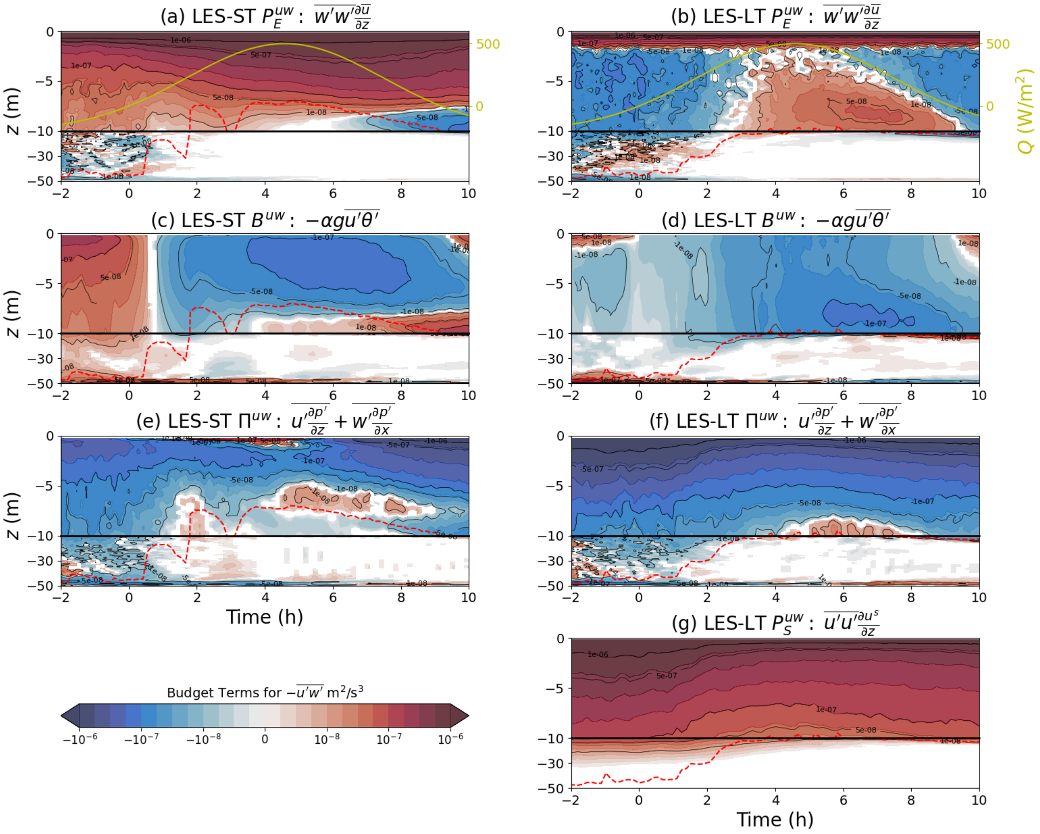

FIG. 7. The evolution of budget terms for along-wind momentum flux $-\overline{u'w'}$ based on LES results, as described in (26): (a, b) production term due to Eulerian shear P_E^{uw}, (c, d) buoyancy term B^{uw}, (e, f) pressure term Π^{uw}, and (g) production term due to Stokes drift shear P_S^{uw} for (left) ST and (right) LT. The Y-axis is divided into two regions, and the red and yellow lines are the same as those in Figure 2. Colors are displayed in logarithmic form and values smaller than 10^{-9} are considered as 0.

Compared to the ST case, B^{uw} for the LT case is smaller, which is opposite of what is observed for B^{TKE}, suggesting that LT leads to weaker turbulent heat transport in the along-wind direction. Nevertheless, for both ST and LT, B^{uw} remains relatively small compared to the major terms, especially near the ocean surface, consistent with the TKE budgets. These small buoyancy terms justify neglecting them in equations (12a)-(12c) of the simplified model for near-surface ocean regions. Notably, neglecting buoyancy does not imply that our model ignores heating effects. Instead, the heating effect is incorporated into l through l_{MO}. This approach implicitly captures heating effects without explicitly including heat flux terms in the budget, for example, it captures the turbulence shutdown due to extreme heating. Specifically, under extremely large heat flux, l becomes very small, leading to large velocity shear and temperature gradients. Since both heat flux and momentum flux are finite, this strong shear results in a thinner boundary layer, indicating a shutdown of turbulence at deeper positions.

In addition to dropping the buoyancy terms in the TKE and momentum budget equations, we also neglect the buoyancy term in the $\overline{\theta' w'}$ budget equation, which motivates an analysis of its budget. Its original budget equation is shown as:

$$\frac{\partial \overline{\theta' w'}}{\partial t} = P_{\theta}^{\theta w} + P_{S}^{\theta w} + B^{\theta w} + \Pi^{\theta w} + SGS. \tag{27}$$

The left-hand side represents the turbulent heat flux temporal changing rate; the first four terms on the right-hand side are related to mean temperature shear, Stokes drift shear, buoyancy, and pressure (see Table 2); the last term, SGS, denotes the sum of subgrid-scale terms and other minor contributions.

For the ST case, the primary production term is $P_{\theta}^{\theta w}$, whereas in the LT case, both $P_{\theta}^{\theta w}$ and $P_{S}^{\theta w}$ contribute significantly (Figure 8). Notably, $P_{S}^{\theta w}$ dominates near the surface, while $P_{\theta}^{\theta w}$ dominates near the DWL base (Figures 8b,d). Although we neglect $B^{\theta w}$ in (12e) in order to derive the solution for the SMC model, it is important to note that while $B^{\theta w}$ is smaller than the dominant production terms, it is more important than B^{uw}.

5. Insights on Mixing Parameterizations

The above section provides evidence for the applicability of our assumptions underlying the simplified SMC model based on LES results and demonstrates qualitative consistency between the LES data and the solution from the simplified model. In this section, we further compare the results from the simplified model with those of LES to provide insights into surface scaling in the presence of LT and heating.

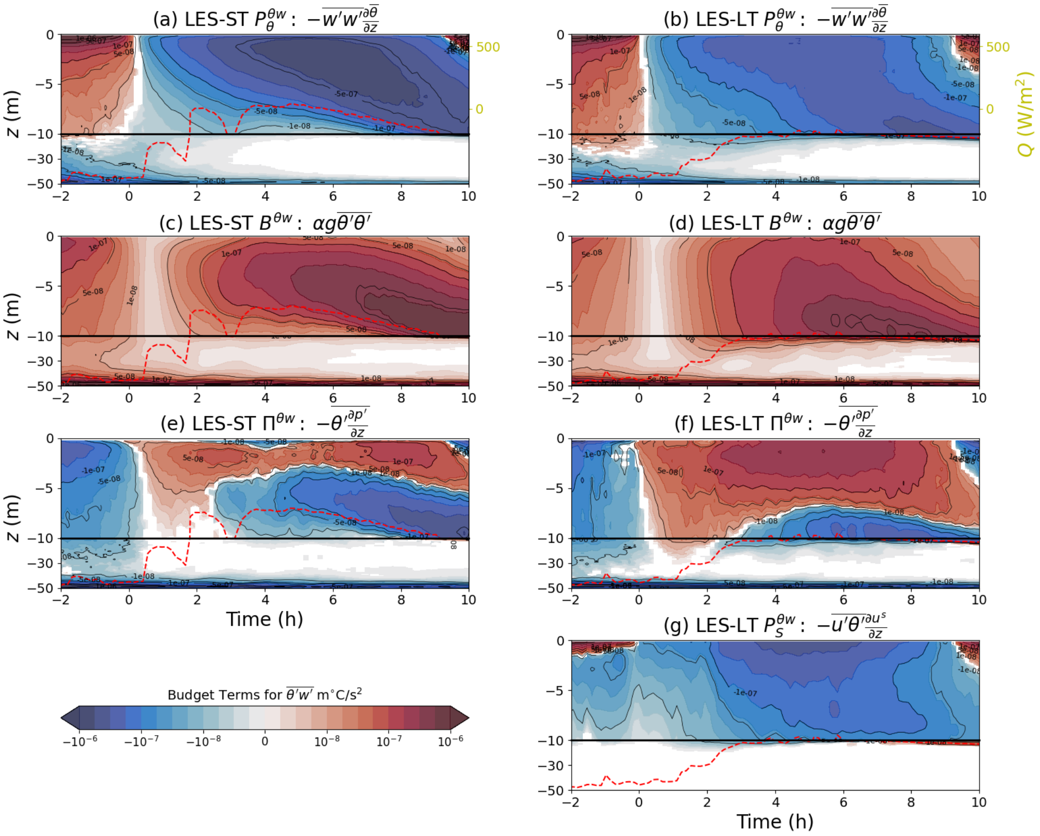

Fig. 8. The evolution of budget terms for turbulent heat flux $\overline{\theta' w'}$ based on LES results, as described in (27): (a, b) production term due to temperature gradient $P_\theta^{\theta w}$, (c, d) buoyancy term $B^{\theta w}$, (e, f) pressure term $\Pi^{\theta w}$, and (g) production due to Stokes drift shear $P_S^{\theta w}$ for (left) ST and (right) LT. The Y-axis is divided into two regions, and the red and yellow lines are the same as those in Figure 2. Colors are displayed in logarithmic form and values smaller than 10^{-9} are considered as 0.

a. Effects of Penetrative Heating and LT on Mixing Length

As we prescribe the mixing length l in the simplified model, it is necessary to determine a reasonable expression for l before comparing the results of the simplified model with those of LES. According to (12a), we calculate the LES mixing length:

$$l = c_\varepsilon \frac{q^3}{\varepsilon}, \tag{28}$$

where q and ε are from LES results. As shown in Figures 3a,b, the LES-derived mixing length, denoted as l^{LES}, increases with depth and decreases with increasing heating. These trends are consistent with l from (13) in our simplified model. Within the DWL, l^{LES} for LT is larger than for ST, as the LT structure usually generates relatively larger eddies, which are associated with a larger mixing length. This suggests a need to consider LT effects when prescribing l in the simplified model.

Figures 9c,d show the ratio of l^{LES} to the prescribed l using MOST coefficient $G_1 = 4.8$. For both ST and LT cases, l^{LES} is significantly larger than the MOST-based l, especially near the ocean surface, suggesting the influence of other factors on the mixing length in addition to LT. Since this deviation is also observed in the ST case, the most likely cause is penetrative heating, where the MOST-based l is applied under surface heating conditions. As shown in Figures 6g,h, the turbulent buoyancy flux B^{TKE} exhibits a convex shape with a small magnitude near the surface. Therefore, using MOST scaling based on surface heat flux may overestimate the heating effects under penetrative heating, leading to an underestimation of l.

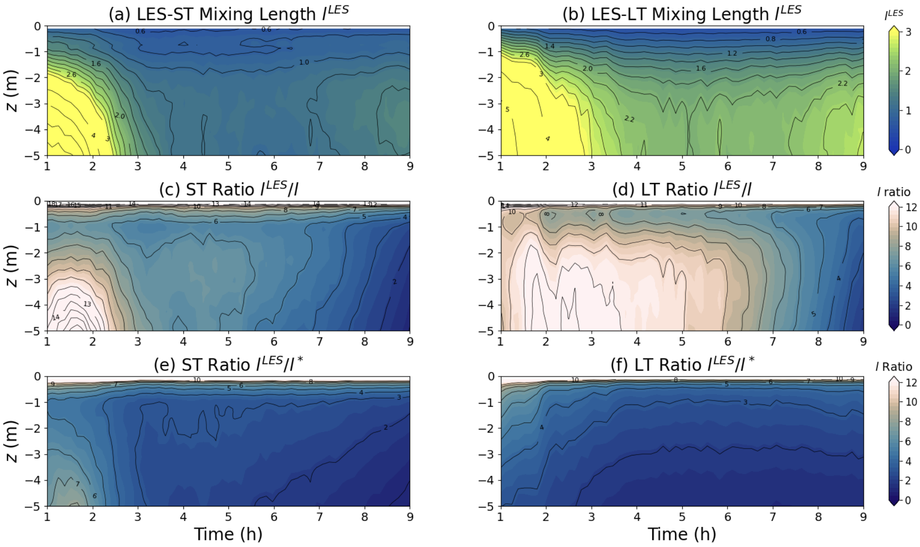

Fig. 9. The (a,b) mixing length based on LES results, l^{LES}, and the ratio of the LES mixing lengths to (c,d) the MOST-based mixing length l (13) and to (e,f) the modified mixing length l^* (29) for the (left) ST and (right) LT cases.

Here, we modify (13) to account for the effects of LT and penetrative heating, resulting in the form:

$$l^* = \frac{\kappa|z|}{1 + \frac{4.8R_h|z|}{l_{MO}(1+La_t^{-2})}}, \tag{29}$$

where R_h represents the reduction in heating effects due to penetrative heat flux (Section 2b), and $1 + La_t^{-2}$ is a factor unifying both ST and LT cases, with a form consistent with Large et al. (2019a).

To validate the modifications for penetrative heating and LT separately, we assess the modified l^* for penetrative heating by comparing the velocity shear predicted by traditional MOST using l^* with LES results for the ST case. As shown in Figure 10a, the velocity shear predicted by traditional MOST aligns with the LES results in terms of evolution, but with larger magnitudes. In contrast, the modified MOST, which incorporates penetrative heating, significantly improves the prediction (Figure 10b). For the ST case, the average DWL depth is approximately 8 m, with an associated R_h value of 0.39 (Figure 10c). The modified MOST captures the substantial reduction in the heating effects due to penetrative heating.

For the assessment of the LT modification, Figures 9e,f compares the ratio of the mixing length from LES and the modified mixing length based on (29). Compared to l without modification (Figures 9c,d), the difference in the ratio between the two cases significantly decreases, indicating that the factor $1 + La_t^{-2}$ successfully accounts for the LT effects. The agreement of l^* with l^{LES} is much improved, although l^* is somewhat smaller. Nevertheless, l^* performs well in the subsequent scaling of mixing coefficients.

b. Scaling for Near-surface Eddy Viscosity and Diffusivity

As suggested in our simplified SMC model, the normalized mixing coefficients can be expressed as functions of η. Using the modified mixing length l^*, we compare $K_{mL}/(u_* l^*)$ and $K_s/(u_* l^*)$ in the near-surface layer between the results from LES and the simplified model. The near-surface layer is defined as $|z| < 0.1h_b$, consistent with the applicable depth range of MOST. The budget analyses have indicated that turbulence in the near-surface layer is in quasi-equilibrium during diurnal heating. Therefore, to include a greater range of LT conditions for testing the general applicability of our mixing parameterization, we utilize the stationary LES experiments listed in Table 2 for this comparison. The first three vertical points near the ocean surface are excluded

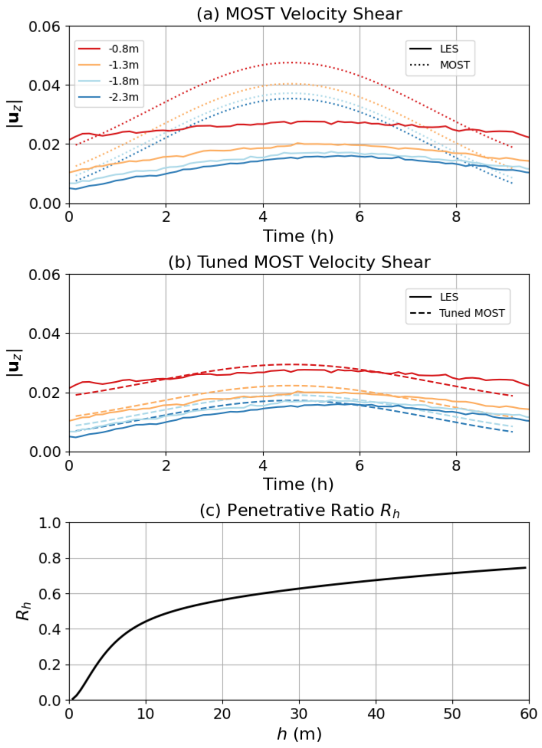

FIG. 10. Comparison of near-surface velocity shear magnitude between LES-ST and the MOST scaling for (a) without and (b) with consideration of penetrative effects. (c) Penetrative ratio R_h for different boundary layer depths.

from the comparison, because small-scale eddies are not sufficiently well resolved very close to the boundary.

The LES-obtained $K_{mL}/(u_* l^*)$ varies by a factor of 2 with η (Figure 11a) but variations are significantly smaller than those of K_s (Figure 11b), suggesting its weak sensitivity to LT effects. The relatively small variation in $K_{mL}/(u_* l^*)$ despite significant changes in Stokes drift shear across different LT strengths suggests a compensating effect between Stokes drift shear and Eulerian velocity shear in the near-surface layer. In contrast, $K_s/(u_* l^*)$ from LES exhibits significant dependence on η, with maximum values up to four times larger than minimum values (Figure 11b). This highlights the pronounced impact of LT on temperature mixing near the ocean surface. Since η reflects the degree of dominance of Stokes drift shear, the result suggests that when Stokes drift shear is sufficiently strong, LT drives mixing, even in the presence of strong stratification.

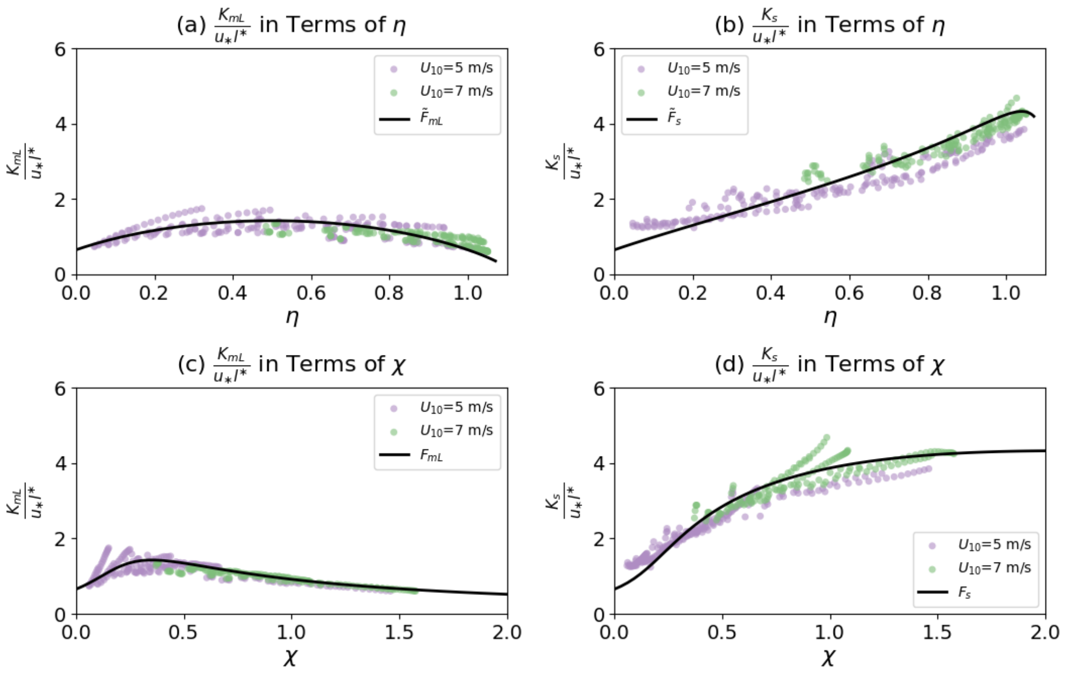

FIG. 11. Comparison of normalized (left) Lagrangian eddy viscosity $K_{mL}/(u_* l^*)$ and (right) eddy diffusivity $K_s/(u_* l^*)$ for surface layer ($|z| < 0.1h_b$) between LES results (points) and solution based on the simplified model (lines). The comparison is shown in terms of (top) η, as described in (16), and (bottom) χ, as described in (15). Colors of the points indicate simulations driven by wind speeds of 5 m/s (purple) and 7 m/s (green). Lines in (a) and (b) are solutions of (23) and (22), respectively, and lines in (c) and (d) are the same solution by expressing η with χ through (16). Notably, we adjust B_1 to 0.51 in the simplified model to set Pr = 1 for ST.

The dependence of the ratio of K_{mL} to $u_* l^*$ and the ratio of K_s to $u_* l^*$ on η is both qualitatively and quantitatively consistent with the relationships derived from the simplified model (Figures 11a,b). Given the varying LT conditions used in these comparisons, the consistency between LES results and the prediction from simplified model further validates the approach for incorporating LT into the mixing length, as shown in (29). Surprisingly, the simplified model for $\tilde{F}_{mL}$, using the constants from Brost and Wyngaard (1978), aligns well with the LES results. Given this strong agreement, we adjust the value of B_1 to 0.51 in $\tilde{F}_s$ to match the ST condition with $Pr = 1$, which also aligns well with LES results.

As shown in (16), η is a function of χ, which is expressed in terms of known variables. Accordingly, we compare the non-dimensional mixing coefficients as function of χ (Figures 11c,d).

The results based on χ are in good agreement with the LES results, indicating the feasibility of near-surface scaling derived from known forcing inputs. This agreement also highlights the dependence of these scalings on the Stokes drift profiles.

To further assess the scaling from the simplified model, we compare its predicted temperature gradient based on different scalings with the LES results. Considering penetrative heating, we assume $-\overline{\theta' w'} + I(z)/(\rho C_p) \approx Q/(\rho_0 C_p)$ in the near-surface layer. The temperature gradient is then calculated as:

$$\frac{\partial \theta}{\partial z} = \frac{I_0 - I(z)}{\rho C_p K_s}. \tag{30}$$

As shown in Figure 12, the prediction based on the simplified model scaling exhibits the best agreement with LES results. In contrast, prediction using traditional MOST scaling typically overestimates the temperature gradient by a factor of $4-5$. Although including modifications for penetrative heating reduces this overestimation, the results remain significantly larger than those from LES. Therefore, these results demonstrate the applicability of the simplified model and highlight the importance of accounting for LT effects in DWLs. Notably, the expressions for the mixing coefficients in the simplified model do not include Coriolis effects, consistent with our results in Appendix A1 that the Coriolis effects are small within the near-surface layer. However, for the parameterization of deeper depths, Coriolis effects may play an important role in the profiles of mixing coefficients (Schmitt et al. 2024).

6. Conclusion

In this study, we use large eddy simulations (LES) to investigate the heated ocean surface boundary layer (OSBL) under the influence of Langmuir turbulence (LT) and evaluate a vertical mixing scheme derived from a simplified second-moment closure (SMC) model.

Driven by diurnal heating, LES results show that the diurnal warm layer (DWL) develops following a rapid shoaling of the ocean surface boundary layer (OSBL) after heating begins. Once formed, the DWL traps heat, intensifying OSBL stratification and impeding downward momentum fluxes, thereby sustaining a shallow, stable layer through the cooling phase. LT strongly influences DWL evolution by enhancing mixing. For example, the formation of DWL takes longer with LT than with shear turbulence (ST, i.e., without waves). Furthermore, LT-induced mixing reduces stratification and velocity shear within the DWL, resulting in lower sea surface temperature and

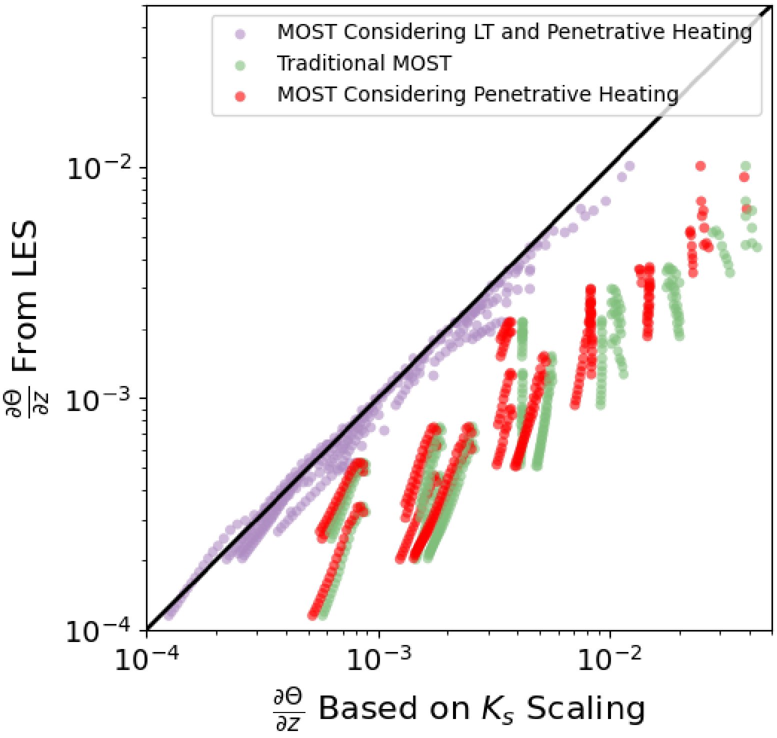

FIG. 12. Comparison of temperature gradient for surface layer ($|z| < 0.1h_b$) between LES results and scaling predictions based on different diffusivity scalings: modified MOST scaling considering LT and penetrative heating effects $K_s = 0.72F_s/F_s(0)u_*l^*$ (purple points), modified MOST scaling only considering penetrative heating effect $K_s = u_*\frac{\kappa|z|}{1+\frac{4.8R_h|z|}{l_{MO}}}$ (red points), and traditional MOST scaling $K_s = u_*\frac{\kappa|z|}{1+\frac{4.8|z|}{l_{MO}}}$. Black line indicates $y = x$.

velocity compared to the ST case. Additionally, the inclusion of Stokes drift shear decreases the turbulent Prandtl number for LT relative to ST, highlighting the need for distinct parameterizations of Lagrangian eddy viscosity and diffusivity.

Budget analyses of various turbulent variables are conducted to investigate their evolution. The turbulent kinetic energy (TKE) budget analysis indicates that turbulence in the DWL adjusts rapidly to diurnal heating, suggesting quasi-equilibrium turbulence. Non-equilibrium turbulence primarily occurs during the initial phase of heating and at greater depths, with insignificant impact on the change of surface velocity and temperature. In the near-surface layer, where Monin-

Obukhov similarity theory (MOST) is typically applied, buoyancy contributions are relatively small compared to the primary budget terms due to penetrative heating. LT exerts a significant influence on these turbulence budgets. For instance, in the ST case, increased velocity shear enhances TKE Eulerian production and dissipation, which does not occur in the LT case due to the dominance of Stokes production. Similarly, Stokes production dominates the budgets for turbulent stress and heat flux, altering the dynamics of these turbulent variables, as also noted in previous studies (e.g., Harcourt 2013; Pearson et al. 2015; Wang and Kukulka 2021).

Building on the LES findings, we propose a simplified SMC model for the near-surface layer, retaining only the leading-order terms and incorporating a mixing length parameter to account for heating effects. The mixing length is derived from MOST with modifications to capture LT and penetrative heating effects, informed by LES results. A key outcome of this model is the extension of traditional MOST to LT conditions, expressed explicitly through the non-dimensional parameter $\frac{l}{u_*}\frac{\partial u^s}{\partial z}$. The solutions of the simplified model effectively explain LES-observed phenomena, such as LT-induced turbulence anisotropy and variations in the turbulent Prandtl number. Furthermore, the near-surface scaling guided by the simplified model successfully reproduces the LES results under a wide range of heating and LT conditions, addressing the consistent overestimation of stratification near the surface observed in traditional MOST scaling.

Recently, several studies have led to comprehensive modifications of the K-profile parameterization model, incorporating the effects of LT (Large et al. 2019a,b, 2021). These modifications include surface scaling, non-local transport, and entrainment/detrainment processes, advocating for separate treatments of these distinct processes. Unlike previous LT parameterizations, our research demonstrates the dependence of near-surface layer scaling on a non-dimensional parameter explicitly expressed by Stokes drift shear. This finding enhances the understanding of OSBL dynamics. The incorporation of this new non-dimensional parameter into OSBL parameterization is poised to improve the accuracy of future models, offering more precise predictions of ocean mixing processes and their interaction with atmospheric forcing.

Acknowledgments. This work is funded by the National Science Foundation Grants OCE-1634578 and OCE-2219825. We would like to acknowledge high-performance computing support from Cheyenne (https:// doi.org/10.5065/D6RX99HX) provided by National Center for Atmospheric Research's Computational and Information Systems Laboratory, sponsored by the National Science Foundation. This research is also supported in part through the use of Information Technologies (IT) resources at the University of Delaware, specifically the high-performance computing resources.

Data availability statement. The numerical results used in this study are simulated by the National Center for Atmospheric Research large eddy simulation model initially established by Moeng (1984) and operated with the numeric scheme of Sullivan et al. (1996). The code and data for Large Eddy Simulation and the derivation of the simplified model solution can be accessed through "https://zenodo.org/records/14699164".

APPENDIX

A1. Influence of Coriolis Force on DWL

In this study, most simulations are conducted at mid-latitudes with Coriolis parameter $f = 0.0001$ 1/s (Table 1). However, recent studies indicate the critical role of the Coriolis force in determining the depth and parameterization of the DWL (Noh and Choi 2018; Wang et al. 2023; Schmitt et al. 2024). However, the scaling of mixing coefficients developed in this study focuses on the near-surface layer, where MOST is typically applicable. Therefore, we conducted sensitivity tests for different Coriolis parameters and found that the Coriolis effects on the near-surface layer are negligible. Figure A1 demonstrates that the vertical gradients of temperature and velocity, along with their associated mixing coefficients, are largely independent of variations in the Coriolis parameter. This limited influence can be attributed to the small length scale and large velocity scale in this region, leading to a large Rossby number, which renders the Coriolis force's effect negligible.

A2. Weakening LT due to Strong Heating

Both the simplified SMC model and transient LES results imply that strong heating may weaken the LT effects. Here we investigate this LT weakening based on stationary LES results, which

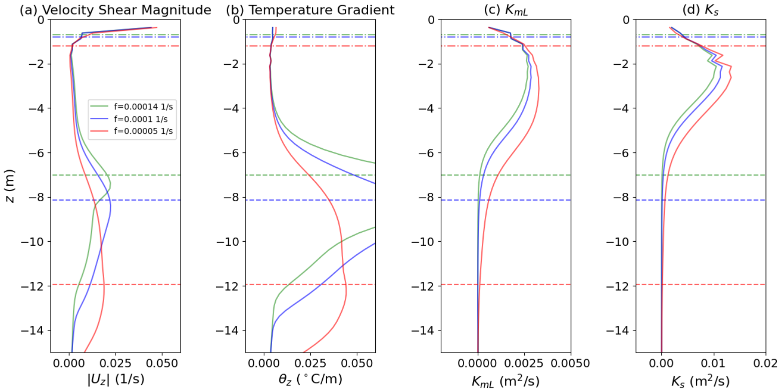

FIG. A1. Profiles of (a) Eulerian velocity shear magnitude, (b) temperature gradient, (c) Lagrangian eddy viscosity K_{mL}, and (d) eddy diffusivity K_s under low (red line), middle (blue line), and high (green line) latitudes. Profiles are based on stationary LES results driven by constant forcing ($u_* = 0.0061$ m/s, $La_t = 0.3$, $Q = 500$ W/m^2). Horizontal lines indicate the mixing layer depths (dashed line) and their 10% positions (dash-dotted line).

provide a wider range of LT conditions. We quantify the dominance of LT by calculating the ratio of Stokes drift production to total TKE production integrated over the mixing layer, denoted as

$$R_{TKE} = \frac{\int_{-h_b}^{0} P_S^{TKE} dz}{\int_{-h_b}^{0} (P_E^{TKE} + P_S^{TKE}) dz}. \tag{A1}$$

Figure A2 shows that for increasing heating (decreasing $l_{MO}/(u_*/f)$), R_{TKE} decreases at constant La_t, indicating that the relative LT strength decreases for strong heating. The change of R_{TKE} is primarily due to the heating-induced jets. Increased heating typically results in shallower and more stratified surface layers, which restrict the vertical mixing, yielding more sheared jets. This enhanced shear amplifies P_E^{TKE}, thereby reducing the relative contribution of P_S^{TKE}, manifesting as LT weakening. Note also that Stokes drift shear production over the OSBL happens in a shallower DWL, which also contributes to reduced LT effects (Harcourt and D'Asaro 2008; Kukulka and Harcourt 2017).

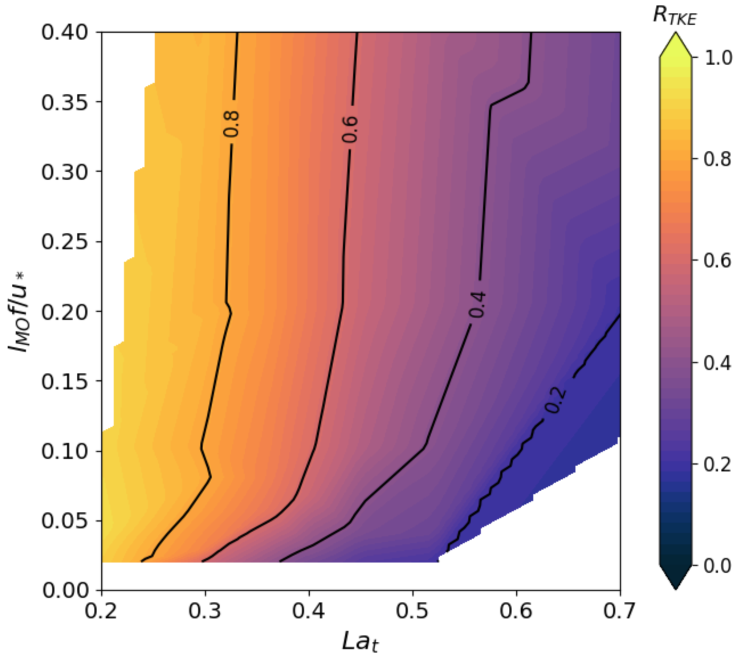

FIG. A2. Distribution of integrated TKE production ratio of Stokes production to total production R_{TKE} as a function of the normalized MO length scale and turbulent Langmuir number La_t.

References

Belcher, S. E., and Coauthors, 2012: A global perspective on langmuir turbulence in the ocean surface boundary layer. *Geophysical Research Letters*, **39 (18)**.

Brost, R., and J. Wyngaard, 1978: A model study of the stably stratified planetary boundary layer. *Journal of Atmospheric Sciences*, **35 (8)**, 1427–1440.

Businger, J. A., J. C. Wyngaard, Y. Izumi, and E. F. Bradley, 1971: Flux-profile relationships in the atmospheric surface layer. *Journal of the atmospheric Sciences*, **28 (2)**, 181–189.

Craig, P. D., 1996: Velocity profiles and surface roughness under breaking waves. *Journal of Geophysical Research: Oceans*, **101 (C1)**, 1265–1277.

Craik, A. D., and S. Leibovich, 1976: A rational model for langmuir circulations. *Journal of Fluid Mechanics*, **73 (3)**, 401–426.

D'Asaro, E. A., J. Thomson, A. Shcherbina, R. Harcourt, M. Cronin, M. Hemer, and B. Fox-Kemper, 2014: Quantifying upper ocean turbulence driven by surface waves. *Geophysical Research Letters*, **41 (1)**, 102–107.

de Boyer Montégut, C., G. Madec, A. S. Fischer, A. Lazar, and D. Iudicone, 2004: Mixed layer depth over the global ocean: An examination of profile data and a profile-based climatology. *Journal of Geophysical Research: Oceans*, **109 (C12)**.

Fairall, C. W., E. F. Bradley, J. Godfrey, G. Wick, J. B. Edson, and G. Young, 1996: Cool-in and warm-layer effects on sea surface temperature. *Journal of Geophysical Research: Oceans*, **101 (C1)**, 1295–1308.

Farmer, D., and M. Li, 1995: Patterns of bubble clouds organized by langmuir circulation. *Journal of Physical Oceanography*, **25 (6)**, 1426–1440.

Foken, T., 2006: 50 years of the monin–obukhov similarity theory. *Boundary-Layer Meteorology*, **119**, 431–447.

Fox-Kemper, B., L. Johnson, and F. Qiao, 2022: Ocean near-surface layers. *Ocean Mixing*, Elsevier, 65–94.

Gargett, A., and C. Grosch, 2014: Turbulence process domination under the combined forcings of wind stress, the langmuir vortex force, and surface cooling. *Journal of Physical Oceanography*, **44 (1)**, 44–67.

Gargett, A., J. Wells, A. Tejada-Martinez, and C. Grosch, 2004: Langmuir supercells: A mechanism for sediment resuspension and transport in shallow seas. *Science*, **306 (5703)**, 1925–1928.

Gargett, A. E., and J. R. Wells, 2007: Langmuir turbulence in shallow water. part 1. observations. *Journal of Fluid Mechanics*, **576**, 27–61.

Grant, A. L., and S. E. Belcher, 2009: Characteristics of langmuir turbulence in the ocean mixed layer. *Journal of Physical Oceanography*, **39 (8)**, 1871–1887.

Harcourt, R. R., 2013: A second-moment closure model of langmuir turbulence. *Journal of Physical Oceanography*, **43 (4)**, 673–697.

Harcourt, R. R., 2015: An improved second-moment closure model of langmuir turbulence. *Journal of Physical Oceanography*, **45 (1)**, 84–103.

Harcourt, R. R., and E. A. D'Asaro, 2008: Large-eddy simulation of langmuir turbulence in pure wind seas. *Journal of Physical Oceanography*, **38 (7)**, 1542–1562.

Högström, U., 1988: Non-dimensional wind and temperature profiles in the atmospheric surface layer: A re-evaluation. *Topics in micrometeorology. A Festschrift for arch dyer*, 55–78.

Hughes, K. G., J. N. Moum, and E. L. Shroyer, 2020a: Evolution of the velocity structure in the diurnal warm layer. *Journal of Physical Oceanography*, **50 (3)**, 615–631.

Hughes, K. G., J. N. Moum, and E. L. Shroyer, 2020b: Heat transport through diurnal warm layers. *Journal of Physical Oceanography*, **50 (10)**, 2885–2905.

Hughes, K. G., J. N. Moum, E. L. Shroyer, and W. D. Smyth, 2021: Stratified shear instabilities in diurnal warm layers. *Journal of Physical Oceanography*, **51 (8)**, 2583–2598.

Kantha, L. H., and C. A. Clayson, 1994: An improved mixed layer model for geophysical applications. *Journal of Geophysical Research: Oceans*, **99 (C12)**, 25 235–25 266.

Kantha, L. H., and C. A. Clayson, 2004: On the effect of surface gravity waves on mixing in the oceanic mixed layer. *Ocean Modelling*, **6 (2)**, 101–124.

Kawai, Y., and A. Wada, 2007: Diurnal sea surface temperature variation and its impact on the atmosphere and ocean: A review. *Journal of oceanography*, **63 (5)**, 721–744.

Kukulka, T., and R. R. Harcourt, 2017: Influence of stokes drift decay scale on langmuir turbulence. *Journal of Physical Oceanography*, **47 (7)**, 1637–1656.

Kukulka, T., K. L. Law, and G. Proskurowski, 2016: Evidence for the influence of surface heat fluxes on turbulent mixing of microplastic marine debris. *Journal of Physical Oceanography*, **46 (3)**, 809–815.

Kukulka, T., A. J. Plueddemann, and P. P. Sullivan, 2013: Inhibited upper ocean restratification in nonequilibrium swell conditions. *Geophysical Research Letters*, **40 (14)**, 3672–3676.

Kukulka, T., A. J. Plueddemann, J. H. Trowbridge, and P. P. Sullivan, 2010: Rapid mixed layer deepening by the combination of langmuir and shear instabilities: A case study. *Journal of Physical Oceanography*, **40 (11)**, 2381–2400.

Large, W. G., J. C. McWilliams, and S. C. Doney, 1994: Oceanic vertical mixing: A review and a model with a nonlocal boundary layer parameterization. *Reviews of geophysics*, **32 (4)**, 363–403.

Large, W. G., E. G. Patton, A. K. DuVivier, P. P. Sullivan, and L. Romero, 2019a: Similarity theory in the surface layer of large-eddy simulations of the wind-, wave-, and buoyancy-forced southern ocean. *Journal of Physical Oceanography*, **49 (8)**, 2165–2187.

Large, W. G., E. G. Patton, and P. P. Sullivan, 2019b: Nonlocal transport and implied viscosity and diffusivity throughout the boundary layer in les of the southern ocean with surface waves. *Journal of Physical Oceanography*, **49 (10)**, 2631–2652.

Large, W. G., E. G. Patton, and P. P. Sullivan, 2021: The diurnal cycle of entrainment and detrainment in les of the southern ocean driven by observed surface fluxes and waves. *Journal of Physical Oceanography*, **51 (10)**, 3253–3278.

Li, Q., and B. Fox-Kemper, 2017: Assessing the effects of langmuir turbulence on the entrainment buoyancy flux in the ocean surface boundary layer. *Journal of Physical Oceanography*, **47 (12)**, 2863–2886.

McWilliams, J. C., E. Huckle, J. Liang, and P. P. Sullivan, 2014: Langmuir turbulence in swell. *Journal of physical oceanography*, **44 (3)**, 870–890.

McWilliams, J. C., E. Huckle, J.-H. Liang, and P. P. Sullivan, 2012: The wavy ekman layer: Langmuir circulations, breaking waves, and reynolds stress. *Journal of Physical Oceanography*, **42 (11)**, 1793–1816.

McWilliams, J. C., and P. P. Sullivan, 2000: Vertical mixing by langmuir circulations. *Spill Science & Technology Bulletin*, **6 (3-4)**, 225–237.

McWilliams, J. C., P. P. Sullivan, and C.-H. Moeng, 1997: Langmuir turbulence in the ocean. *Journal of Fluid Mechanics*, **334**, 1–30.

Min, H. S., and Y. Noh, 2004: Influence of the surface heating on langmuir circulation. *Journal of physical oceanography*, **34 (12)**, 2630–2641.

Moeng, C.-H., 1984: A large-eddy-simulation model for the study of planetary boundary-layer turbulence. *Journal of the Atmospheric Sciences*, **41 (13)**, 2052–2062.

Monin, A., and A. Obukhov, 1954: Osnovnye zakonomernosti turbulentnogo peremeshivanija v prizemnom sloe atmosfery (basic laws of turbulent mixing in the atmosphere near the ground). *Trudy geofiz. inst. AN SSSR*, **24 (151)**, 163–187.

Moulin, A. J., J. N. Moum, and E. L. Shroyer, 2018: Evolution of turbulence in the diurnal warm layer. *Journal of Physical Oceanography*, **48 (2)**, 383–396.

Noh, Y., and Y. Choi, 2018: Comments on “langmuir turbulence and surface heating in the ocean surface boundary layer”. *Journal of Physical Oceanography*, **48 (2)**, 455–458.

Noh, Y., G. Goh, S. Raasch, and M. Gryschka, 2009: Formation of a diurnal thermocline in the ocean mixed layer simulated by les. *Journal of Physical oceanography*, **39 (5)**, 1244–1257.

Paulson, C. A., and J. J. Simpson, 1977: Irradiance measurements in the upper ocean. *Journal of Physical Oceanography*, **7 (6)**, 952–956.

Pearson, B. C., A. L. Grant, J. A. Polton, and S. E. Belcher, 2015: Langmuir turbulence and surface heating in the ocean surface boundary layer. *Journal of Physical Oceanography*, **45 (12)**, 2897–2911.

Plueddemann, A., and J. Farrar, 2006: Observations and models of the energy flux from the wind to mixed-layer inertial currents. *Deep Sea Research Part II: Topical Studies in Oceanography*, **53 (1-2)**, 5–30.

Plueddemann, A. J., J. A. Smith, D. M. Farmer, R. A. Weller, W. R. Crawford, R. Pinkel, S. Vagle, and A. Gnanadesikan, 1996: Structure and variability of langmuir circulation during the surface waves processes program. *Journal of Geophysical Research: Oceans*, **101 (C2)**, 3525–3543.

Price, J. F., R. A. Weller, and R. Pinkel, 1986: Diurnal cycling: Observations and models of the upper ocean response to diurnal heating, cooling, and wind mixing. *Journal of Geophysical Research: Oceans*, **91 (C7)**, 8411–8427.

Prytherch, J., J. T. Farrar, and R. A. Weller, 2013: Moored surface buoy observations of the diurnal warm layer. *Journal of Geophysical Research: Oceans*, **118 (9)**, 4553–4569.

Reichl, B. G., D. Wang, T. Hara, I. Ginis, and T. Kukulka, 2016: Langmuir turbulence parameterization in tropical cyclone conditions. *Journal of Physical Oceanography*, **46 (3)**, 863–886.

Schmitt, M., H. Pham, S. Sarkar, K. Klingbeil, and L. Umlauf, 2024: Diurnal warm layers in the ocean: Energetics, nondimensional scaling, and parameterization. *Journal of Physical Oceanography*, **54 (4)**, 1037–1055.

Skyllingstad, E. D., and D. W. Denbo, 1995: An ocean large-eddy simulation of langmuir circulations and convection in the surface mixed layer. *Journal of Geophysical Research: Oceans*, **100 (C5)**, 8501–8522.

Soloviev, A., and R. Lukas, 1997: Observation of large diurnal warming events in the near-surface layer of the western equatorial pacific warm pool. *Deep Sea Research Part I: Oceanographic Research Papers*, **44 (6)**, 1055–1076.

Soloviev, A., and R. Lukas, 2013: *The near-surface layer of the ocean: structure, dynamics and applications*, Vol. 48. Springer Science & Business Media.

Sullivan, P. P., J. C. McWilliams, and C.-H. Moeng, 1996: A grid nesting method for large-eddy simulation of planetary boundary-layer flows. *Boundary-Layer Meteorology*, **80 (1)**, 167–202.

Sutherland, G., L. Marié, G. Reverdin, K. H. Christensen, G. Broström, and B. Ward, 2016: Enhanced turbulence associated with the diurnal jet in the ocean surface boundary layer. *Journal of Physical Oceanography*, **46 (10)**, 3051–3067.

Terray, E. A., M. Donelan, Y. Agrawal, W. Drennan, K. Kahma, A. J. Williams, P. Hwang, and S. Kitaigorodskii, 1996: Estimates of kinetic energy dissipation under breaking waves. *Journal of Physical Oceanography*, **26 (5)**, 792–807.

Thorpe, S., 2004: Langmuir circulation. *Annual Review of Fluid Mechanics*, **36 (1)**, 55–79.

Van Sebille, E., and Coauthors, 2020: The physical oceanography of the transport of floating marine debris. *Environmental Research Letters*, **15 (2)**, 023 003.

Wang, X., and T. Kukulka, 2021: Ocean surface boundary layer response to abruptly turning winds. *Journal of Physical Oceanography*, **51 (6)**, 1779–1794.

Wang, X., T. Kukulka, J. T. Farrar, A. J. Plueddemann, and S. F. Zippel, 2023: Langmuir turbulence controls on observed diurnal warm layer depths. *Geophysical Research Letters*, **50 (10)**, e2023GL103 231.

Wang, X., T. Kukulka, and A. J. Plueddemann, 2022: Wind fetch and direction effects on langmuir turbulence in a coastal ocean. *Journal of Geophysical Research: Oceans*, **127 (5)**, e2021JC018 222.

Webster, P. J., C. A. Clayson, and J. A. Curry, 1996: Clouds, radiation, and the diurnal cycle of sea surface temperature in the tropical western pacific. *Journal of Climate*, **9 (8)**, 1712–1730.

Weller, R. A., and S. P. Anderson, 1996: Surface meteorology and air-sea fluxes in the western equatorial pacific warm pool during the toga coupled ocean-atmosphere response experiment. *Journal of Climate*, **9 (8)**, 1959–1990.

Weller, R. A., J. P. Dean, J. F. Price, E. A. Francis, J. Marra, and D. C. Boardman, 1985: Three-dimensional flow in the upper ocean. *Science*, **227 (4694)**, 1552–1556.

Wyngaard, J. C., 2010: *Turbulence in the Atmosphere*. Cambridge University Press.

Zheng, Z., 2023: Impacts of surface waves on turbulence in ocean surface boundary layers: Observations and scaling. Ph.D. thesis, University of Washington.

Zheng, Z., R. R. Harcourt, and E. A. D'Asaro, 2021: Evaluating monin–obukhov scaling in the unstable oceanic surface layer. *Journal of Physical Oceanography*, **51 (3)**, 911–930.